Final Scientific Report

Project Title: **"Demonstration of Next-Generation PEM CHP Systems for Global Markets Using PBI Membrane Technology"**

Project Period: January 1, 2007 to April 30, 2009

Date of Report: August, 2009

Recipient: Plug Power Inc.
968 Albany Shaker Road
Latham, NY 12110

Award Number: DE-FG36-07GO17016

Working and Cost Sharing Partners: BASF Fuel Cell, ETEK

Contact: Principal Investigator
John Vogel
518-783-0937
john_vogel@plugpower.com

Program Manager
Katrina Fritz Intwala
518-783-0369
katrina_fritzintwala@plugpower.com

DOE Manager: Jason Marcinkoski
202-586-7466
jason.marcinkoski@ee.doe.gov

DOE Project Officer: Reginald Tyler
303-275-4929; Fax: 303-275-4753
reginald.tyler@go.doe.gov

Project Objective:
Plug Power Inc. (Plug Power), in response to Topic 7B of DOE Funding Opportunity Announcement DE-PS36-06GO96017, has executed an international development and demonstration project within the framework of the existing European Union (EU) – United States (US) Cooperation Agreement on fuel cells. The design, test and validation of a micro-CHP proton exchange membrane (PEM), stationary fuel cell system has advanced the state of the art of high-temperature PEM fuel cell technologies, and has brought a domestic fuel cell heating appliance (FCHA) system design one step closer to commercialization.

Background:
Plug Power and BASF have conducted eight years of development work prior to this project, demonstrating the potential of PBI membranes to exceed many DOE technical targets. This project consisted of:

1. The development of a worldwide system architecture
2. Stack and balance of plant module development
3. Development of an improved, lower cost MEA electrode
4. Receipt of an improved MEA from the EU consortium
5. Integration of modules into a system
6. Delivery of system to EU consortium for additional integration of technologies and testing.

It has been successful in all aspects of development and has satisfactorily achieved its objectives.

Results by Task:

<u>Task 1: Modular/Scaleable Fuel Cell Design – Plug Power</u>

Development of a worldwide system architecture began with the exploration of a variety of factors. System direct material cost (DMC) projections, output size, markets, current technologies and existing consumer data were all used to determine the best size for the DOE/FP6 point product and how this technology scales up and down from this point.

Additionally, factors such as CHP utilization, types of electrical output (50/60 Hz), certification requirements (FCC, CE, UL), indoor/outdoor installation, duty cycles and other operating requirements were evaluated.

The team's first step was to determine an accurate cost projection for the scaleable technology. To do this we used our prototype system developed under a NIST ATP program as a baseline and evaluated costs based on industry standard cost/volume curves appropriate to each component. That is; different components from different industries have different cost/volume relationships.

After developing a projected cost curve for the scalable technology, we normalized the data for annual volume quantities of ten thousand systems. Since there was such a dependence on base assumptions such as the future cost of platinum and the performance of the MEA, we bracketed the analysis with a high and low estimate for the FCHA. Figure 1 shows the FCHA technology scaled from 1 kW to 12; the most likely bracket for this technology. These results were compared with generators.

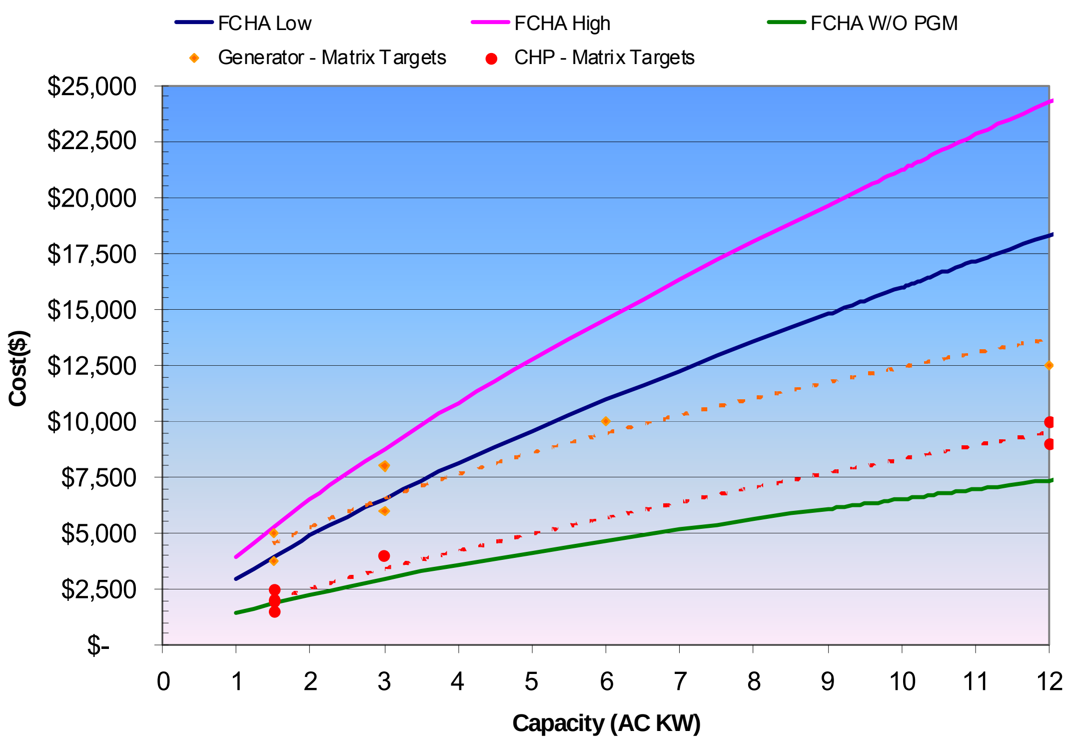

Figure 1: Cost vs. Capacity for FCHA and Generators

Added to this representation was a reference plot of the FCHA without the stack showing the dependence of system DMC on stack size. Notice the almost linear trend as more cells are added to the stack. This is unlike generators which have the same number of parts as the systems scale, just their size changes. This is very important to take into consideration during competitive system sizing.

Another critical characteristic in sizing is utilization. For a CHP system both thermal and electrical utilization needs to be considered. By employing a variety of US and EU user profiles and mapping their utilization a series of return on investment (ROI) curves were generated. The object being to determine for a given user profile, what size system gives the shortest ROI.

We found that the larger systems (> 3 kW) do not operate in the high electrical output mode very often so the customer has a lot of extra fuel cell paid for that isn't being used. The team determined that for single and multifamily use (up to eight family dwellings) the most applicable product would be 3 kW. This had on average, the highest utilization and the lowest ROI. See Figure 2.

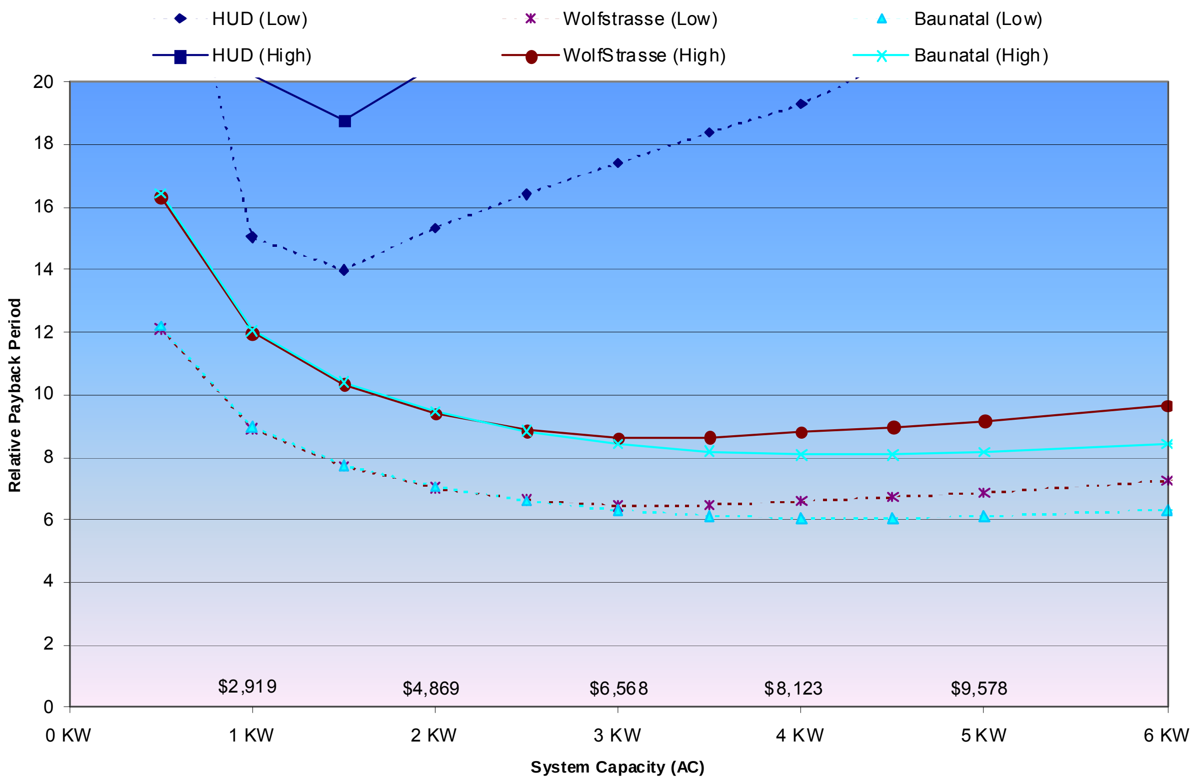

Figure 2: ROI vs. System Capacity for US and EU Customers

During the early phases of worldwide system architecture development Plug Power focused on the exploration of a factors such as system direct material cost (DMC), system capacity, and target markets by intersecting those factors with targeted customer profiles for both electrical and thermal demand. Both large and small residential units of a single and multi-family nature were evaluated to determine an optimum product configuration. It became apparent that the relationship between the electrical demand and the thermal demand defined the effectiveness of a fuel cell heating appliance in given application; This relationship was effected by building size, number of residents, geographic location or climate zone, as well as the year of construction and of course the habits of the residents. A simple model was developed from this work to estimate monthly energy cost savings based on those key factors.

A close examination of the system cost functions indicated the strong linearization of the cost-volume curve was dominated by stack costs. Plug Power focused on an architectural concept where the majority of the system would remain the same with only the power generation or stack component changing; System models and performance projections were established around a “common” system with three different size stacks as options to customize based on expected operational profiles. Stylized version of the three different performance projections can be seen in Figure 3.

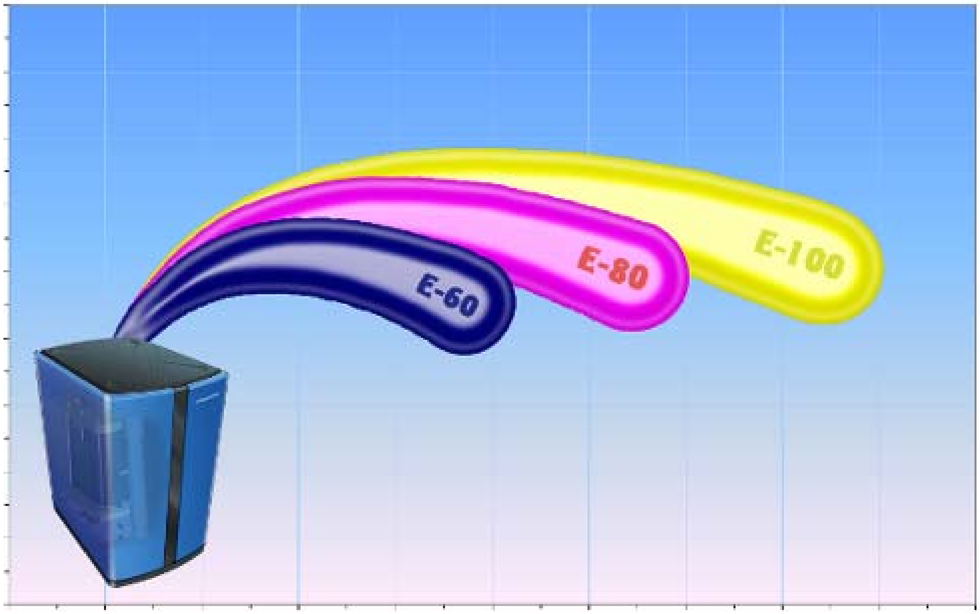

Figure 3: Projected Performance Curves for Fuel Cell Heating Appliance(s)

These curves highlight that fact that a larger stack is not only capable of producing more power, but that it also will operate “higher up” on the polarization curve and therefore produce power more efficiently than a smaller stack. However, this improved efficiency comes at a higher cost, and will not improve the return on investment for all applications, depending primarily on the magnitude of thermal demand and ratio of existing fuel and electricity costs.

Plug Power identified that most applications will require more thermal capacity than that resulting from waste heat of the fuel cell stack during portions of the year whether these demands be short-term daily demands associated with recovery time demands on the domestic hot water system required to support multiple, sequential hot showers; or from sustained cold weather periods requiring extended operation at very high thermal setpoints. Figure 4 serves to estimate thermal demands, demonstrating a reverse cumulative histogram; showing the percentage of time where thermal demands are in excess of a particular point. For example ~85% of the time more than zero kilowatts are required and about 12% of the time a small house requires more than ten kilowatts of heating capacity

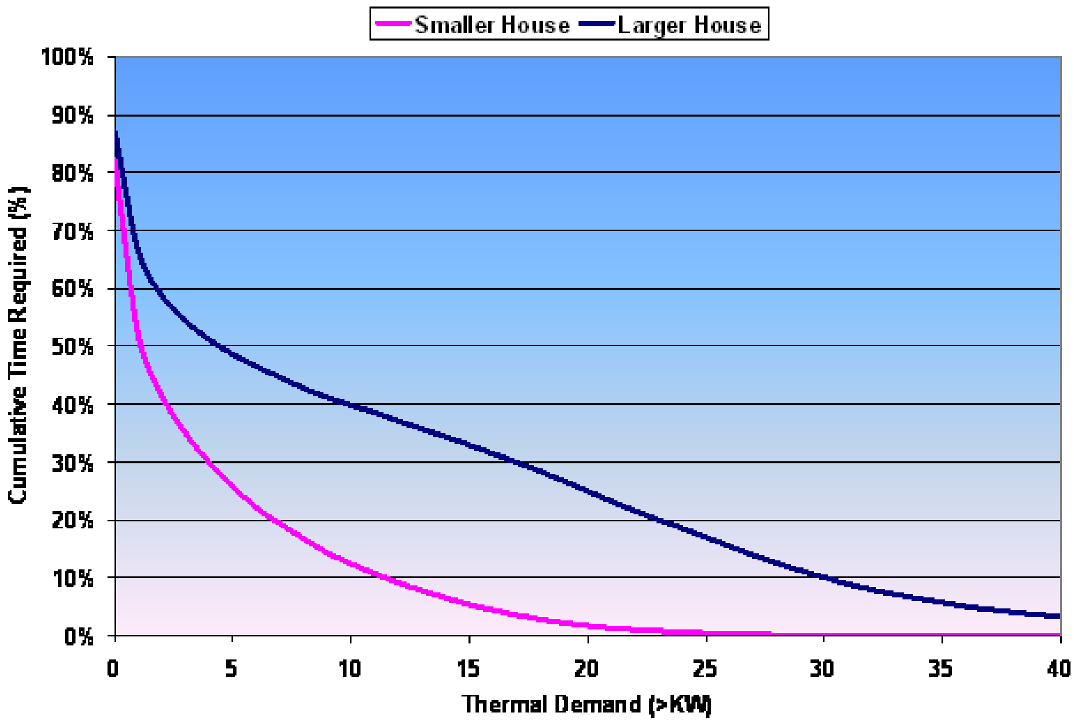

Figure 4: Thermal Requirements for Residential Applications

Based on these assessments of thermal demands, Plug Power has integrated peak heating functionality into the product platform. The traditional ATO or anode tail gas oxidizer has been combined with a pre-mix burner assembly to provide for supplemental heating capacity up to 35kW total to be supplied from the fuel cell heating appliance. This transformation presents the fuel cell heating appliance as a replacement for a traditional heating system rather than a separate component. The incremental cost of adding this functionality to the system add value to the architecture and result it improved economics to the end customer, as well as paving the road for optimal integration of a fuel cell with heating systems by reducing the number of configuration variables encountered.

Task 2: Catalyst Development – ETEK

The basis for creating more stable supported catalysts lies in the choice of carbon support. In general, the more graphitic the support, the more resistant to oxidative corrosion (oxidation of carbon to CO2). Our first subtask was to evaluate numerous carbon supports containing carbon at various levels of graphite content. A number of carbon supports have been tested for corrosion resistance under the following

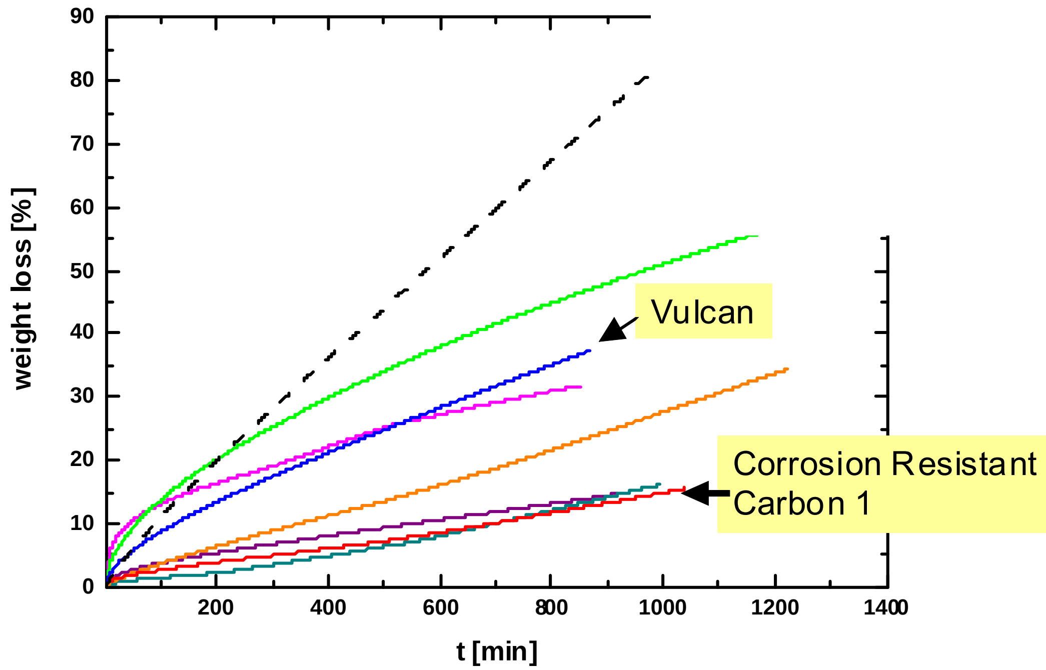

Figure 5: Corrosion Rate in Wt% for Several Carbon Samples at 180 ^oC, 1.0 Volts

condition: an E-TEK ELAT® prepared with the carbon and a binder is subjected to a test whereby a standard E-TEK Pt ELAT acts as both counter & reference electrode. The testing condition is chronocoulometric by stepping the testing electrode, equilibrated at 180 deg C, from resting potential to 1.0 volts for a duration of time and the charge consumed is recorded. It is assumed that most charge is used to oxidize carbon to CO_2. Figure 5 shows the results for a number of carbon supports.

As Figure 5 indicates there are three carbon supports that showed the lowest corrosion rates that are significantly lower than Vulcan. Among these, corrosion resistant carbon 1 exhibited the best surface properties and other physical properties for formulation and electrode preparation.

We prepared numerous alloys of Pt containing Co, Ni, Fe, Vn, and Cr, or ternary combinations thereof. Of these, Pt alloy(I) on corrosion resistant carbon 1 was prepared and compared with presently used Pt alloy in 180 ^oC H_2/O_2 cells. Pure oxygen is selected to accelerate corrosion processes. The performances of the two were very similar but the potential cycling testing between 0.85 and 0.6 volts showed Pt alloy(I) on corrosion resistant carbon 1 had much better stability to potential cycling (180 ^oC, ambient pressure, H_2/O_2). The performance stability comparison is illustrated in Figure 6 whereby the high temperature MEA now containing either presently used Pt alloy on Vulcan (Benchmark) or Pt alloy(I) on Carbon 1 is subjected to potential cycling, (2 hours at 0.85 and 0.6 volts alternatively), and the relative current measured at 0.6V is recorded.

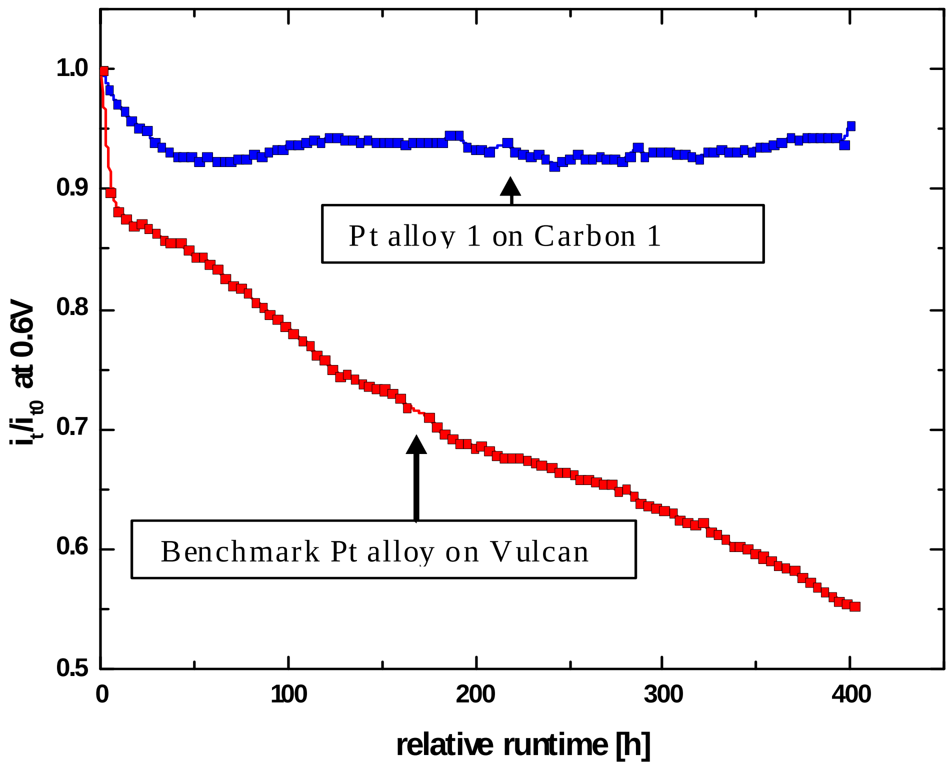

Figure 6: Relative Current Density at 0.6 Volts During Potential Cycling Test for Presently Used Pt Alloy on Vulcan or Pt Alloy(I) on Corrosion Resistant Carbon 1

A key difference for these two carbons is the percentage of graphitization. X-ray diffraction (XRD method) can be used to compare the graphitic content of different carbon supports. Figure 7 compares the XRD graphs of Vulcan and corrosion resistant carbon 1. One can readily distinguish the highly ordered graphitic nature of carbon 1, shown as sharp peaks at two-theta 24 degrees (and other regions) to the more amorphous character, shown most commonly as a broad diffraction pattern at two theta 24.

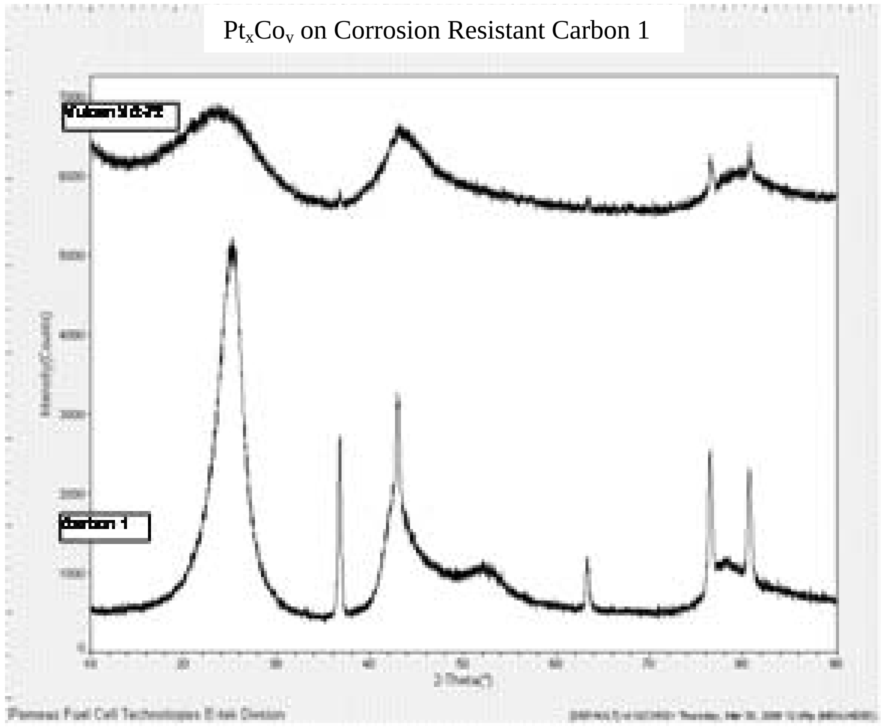

Figure 7: XRD Graphs of Vulcan XC-72 and Carbon 1

In the course of this task we identified three potential graphitic supports and selected two for use as catalyst supports. Using these two supports we developed numerous catalysts and narrowed the field to three catalysts: Pt alloy(I) on Carbon 1, Pt alloy(I) on Carbon 2, and Pt alloy(II) on Carbon 1. These three candidates were passed to the electrode development team of Task 3.

Task 3: Cathode Development – ETEK

Optimize Electrode Structure/Prototype Scale

The main objective of this task was to increase the power output using Task 2's new carbon/catalyst systems through optimization of the cathode structure. For the Celtec® P-1000 MEA, wicking of phosphoric acid into the electrode layer and forming a three phase interface critically controls performance. This wicking is determined by the total hydrophobicity of the catalyst layer, and in turn the catalyst layer hydrophobicity is controlled by the nature of the carbon support and level and type of binding agent (for example, PTFE, popularly called "Teflon®"). We have found that the graphitic nature of the support (Carbon 1, Carbon 2) significantly shifts the innate hydrophobicity of the electrode structure and dramatically impacts the degree and rate of wicking. A Design of Experiment (DoE) was constructed for each of the three prime catalyst systems whereby levels of PTFE were varied and MEAs evaluated. After testing we found that in small scale systems using batch coating methods, GDEs employing Pt alloy(I) on Carbon 2 was roughly equivalent to Pt alloy(II) on Carbon 1, and both of these were slightly better than Pt alloy(I) on Carbon 1. Based on this testing, Pt alloy(I) on Carbon 2 was recommended to the machine coating activities below.

GDL Stability

It is expected that the most sensitive area for degradation is the catalyst/electrode layer. However, as the underlying Gas Diffusion Layer (GDL) is a critical support for the electrode layer, there is a possibility that the carbon of the microporous layer will be subjected to corrosion. As part of this task, we refined the microporous layer of the GDL by incorporating Carbon 1 into the structure.

Construct machine Gas Diffusion Electrode (Cathode)

In this task we outline the use of batch coating machines to produce limited samples for evaluation and optimization. The next scale for electrode fabrication is the use of the roll-to-roll coating machine, as this methodology will be used for delivering demonstration scale volumes of materials, and represents a “manufactured technology.”

A roll-to-roll coating machine demands significantly greater catalyst than the prototype scale device, and the first subtask is to scale from the 20-50g range of Task 2.0 to 500 gram preparations. All three catalysts identified were successfully scaled to 500 gram preparations whereby a sensitivity analysis was performed to link catalyst quality with process conditions.

Secondly, the formulations used at the prototype scale do not have to be robust, since they are used in a singular manner immediately after preparation. For continuous coating, formulation criteria are more demanding, as stability of the suspension is critical. Furthermore, we found that standard formulations used with the new graphitic supports and alternative binder levels were not stable, so several activities were pursued to bring the new materials up to acceptance specifications for coating. Changes in formulation, while helping coating quality, also impacted the GDL/GDE structure, so an optimization cycle was performed through testing materials at the 50 cm^2 single cell level.

During this optimization process we discovered that the system identified as Pt alloy(I) on Carbon 2 was highly sensitive to oven sintering conditions, a critical step in fixing the PTFE binder. We dedicated significant time to identifying the factors leading to a high variation in the performance of assemblies made with this system. While the Pt alloy(I) on Carbon 2 system offers potential, we changed our focus to Pt alloy(II) on Carbon 1, and identified a unique set of conditions that provides acceptable variation during the oven steps, without loss of performance. Pt alloy(II) on Carbon 1 has been recommended for the next phase of Electrode Scale up of Task 5.

Task 4: Anode Pt Reduction – ETEK

In this task we began work on lowering precious metal content in the anode. The first step was to determine the sensitivity of anode performance to precious metal loading when using our standard electrode structure. Figure 8 shows three polarization curves taken with anodes made on our roll-to-roll coating machine using a standard high temperature anode structure. We note that with this structure, there is a large sensitivity of performance to precious metal loading. Given the focus on cathode development for this program, if there is time remaining we will pursue alternative structures and catalysts that may allow reduction of precious metal loading in anodes.

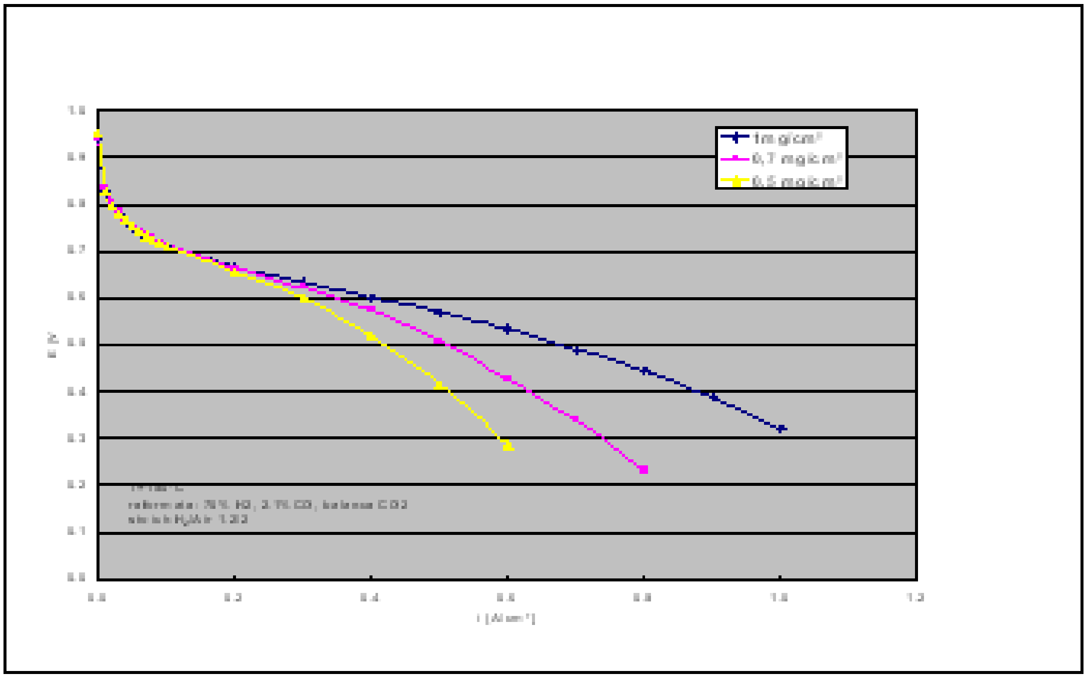

Figure 8: Polarization Curves as a Function of Pt Loading

<u>Task 5: Electrode Scale-Up – ETEK</u>

Activities for Task 5 included: increase the length of coated material, scale sintering from smaller ovens to full size batch production oven, and solve an unexpected issue in laminating critical internal gaskets to Gas Diffusion Electrodes.

We made the first critical jump in scale from a batch coating process to one of our roll-to-roll coating machines, whereby we coated the carbon cloth based gas diffusion layer with Pt alloy (II) on Carbon 1 for approximately 10 linear meters – the shortest reasonable length to obtain steady-state in the machine. We systematically increased the length of coating from 10 linear meters to 25, 50, and finally 70 linear meters. For each increase in length, we measured key parameters such as precious metal distribution/uniformity and ink stability. We were able to produce 70 linear meter coating runs and remain within QC specifications. This final length represents the minimum batch size useful for manufacturing.

Similarly, we had previously used smaller sintering ovens in order to more closely control the temperature and atmosphere within the oven. We mapped temperature profiles within the large format sintering oven, and outfitted the exhaust with an oxygen detector to verify achieving low oxygen content during inert gas operations. Armed with the temperature map, thermal rates, and oxygen measurement during inert operations, we created process conditions that most closely matched those created in the smaller oven. We have currently achieving uniform sintering with batch sizes 33% maximum capacity, and plan to increase this amount going forward.

Lastly, once we started to produce larger batches of cathode gas diffusion electrode with the optimized formulations and process conditions, and larger batches of membrane electrode assemblies were fabricated, a critical property was absent for some of the materials produced. The sub gasket used for creating a sealing area against primary gaskets did not always laminate successfully to some of the gas diffusion electrodes. Working with the BASF Fuel Cell team in Frankfurt, Germany, we identified the reasons and modified the structure of the gas diffusion electrode with a proprietary additive, and re-optimized the formulation to account for this new additive.

The final steps for this task was to confirm multiple coating runs at 70 linear meters, and scale the batch sintering to 50-75% maximum capacity.

Having selected Alloy (II), carbon (2) for scale up, we used our remaining time to reproduce coating runs and test sintering at 50% maximum capacity. We were able to replicate the coating trials (3x repeat) within QC specifications and achieved reasonably low variation for sintering at 50% maximum capacity.

Task 6: Stack Development – Plug Power

This task incorporated a variety of initiatives designed to improve stack performance, life and manufacturability.

Single Pass/Double Pass

Screening testing prior to detailed analysis was conducted to evaluate the effects of a single vs. double pass anode flowfield. The baseline plate design used a 2-pass design on the anode flow field which recombined the anode flow to re-distribute and homogenize the H2 concentration in the reformate; the purpose being to optimize fuel efficiency. This has not proven to be the case with the testing of manufactured plates. It is believed that while 2-pass is thermodynamically correct, we cannot hold the manufacturing tolerances required to maintain a 2-pass orientation with our current material and design. Fuel leaks from the entrance to the exit of the anode, short-circuiting the flowfield. The purpose of this test was to compare the efficiency of a 16-cell stack with the anode running in the baseline 2-pass design with a one of a single pass design.

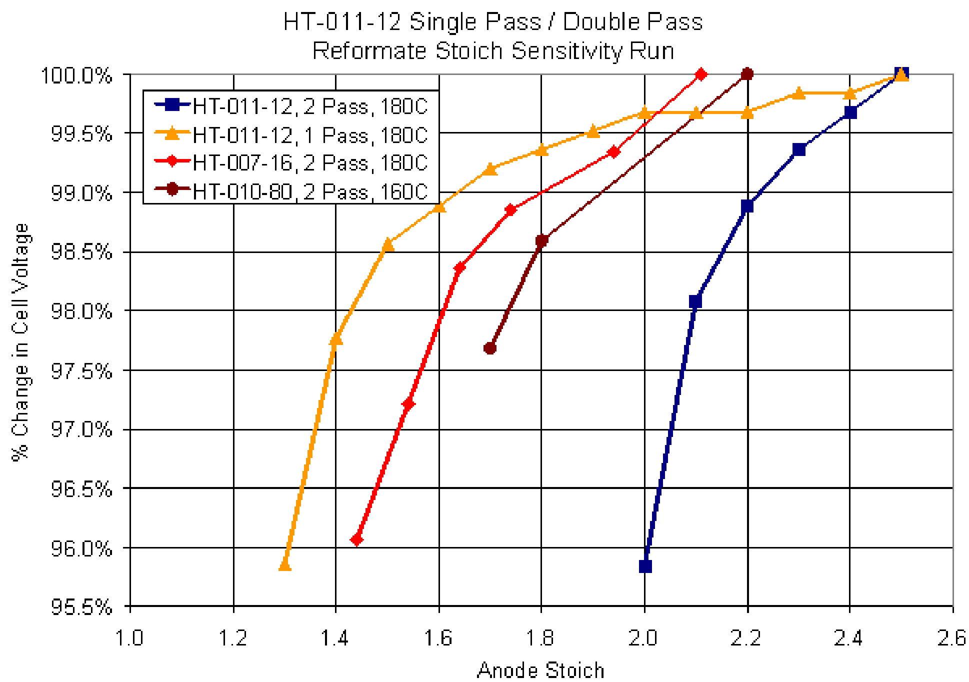

Figure 9: Single Pass/Double Pass Screening Testing

The single pass data collected showed promising results when compared with previous baseline double pass data at various operating conditions. The test was conducted on modules with both configurations. Through the comparison on stoich requirement and cell voltage distribution, the anode flow field impact was studied and the final selection of the anode flow field orientation was made.

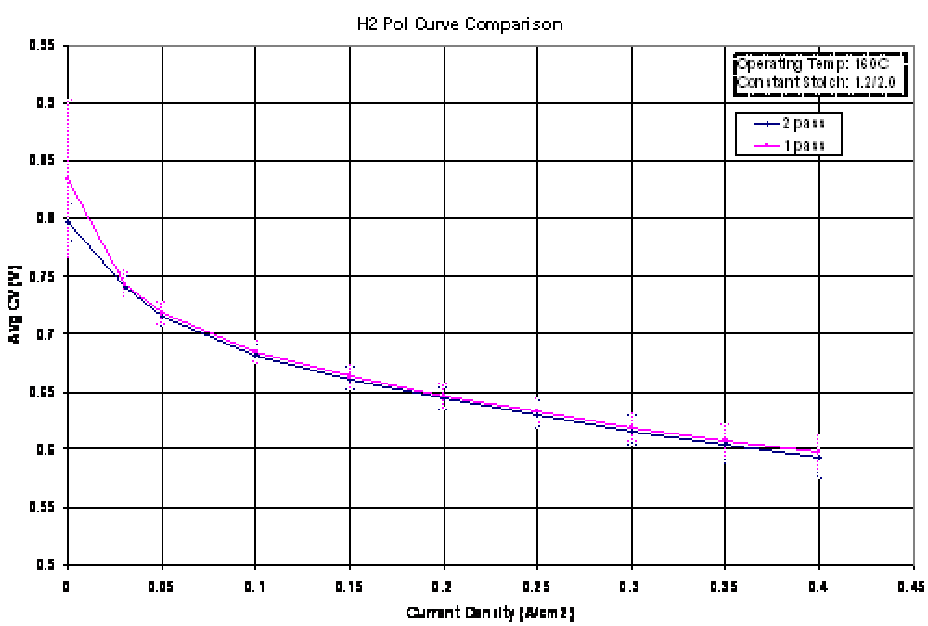

Figure 10: Polarization Curve of Both Anode Gas Flow Orientations.

Hydrogen Polarization Curve: A module was incubated at 1.2/2.0 at 0.2A/cm^2 at 160°C on dry hydrogen and air. Following incubation, a single pass test plan was performed. All tests were performed with humidified anode gas, the results were analyzed and the hydrogen polarization curve is show in Figure 10. There was no significant difference observed from the hydrogen polarization curve between the single and the double pass orientation. Other than the 50mV difference at OCV, the results suggested that the orientation of anode gas flow has no direct impact on the performance of MEA.

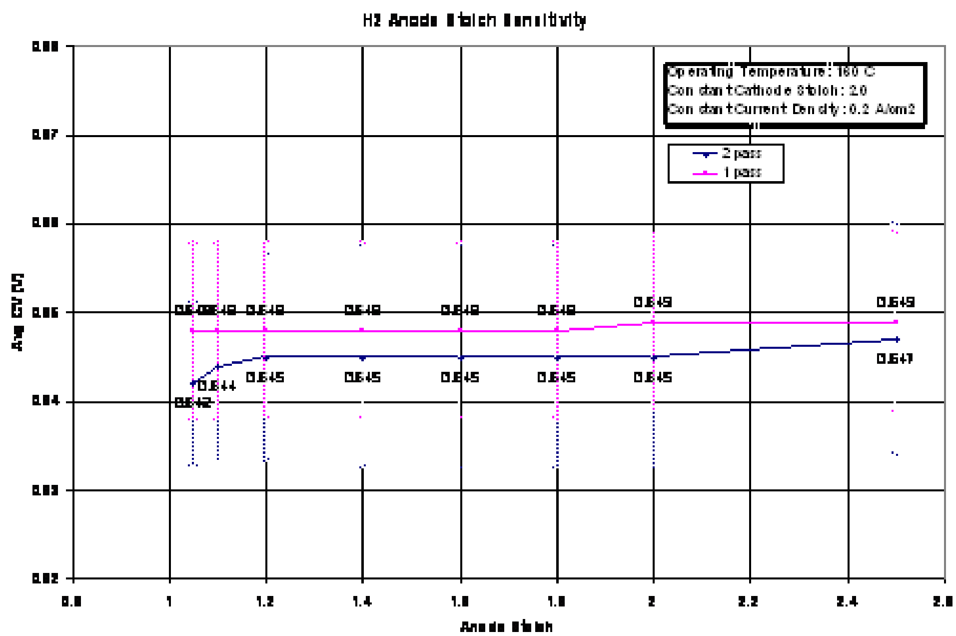

Figure 11: H_2 Anode Stoich Sensitivity Comparison.

Hydrogen Anode Stoich Sensitivity: Following the MEA performance characterization, the BOL test plan called for anode stoich sensitivity test which begin the first part of the fuel utilization characterization. Both setups was performed under identical temperature, cathode stoich and loading.

From Figure 11, one can clearly notice that increasing the anode stoich has no significant improvement on module performance. There is only approximately 1mV difference between operating at 1.05 and 2.5 hydrogen stoich. However, a 1-pass setup does have a 3mV advantage on cell voltage production over 2-pass setup.

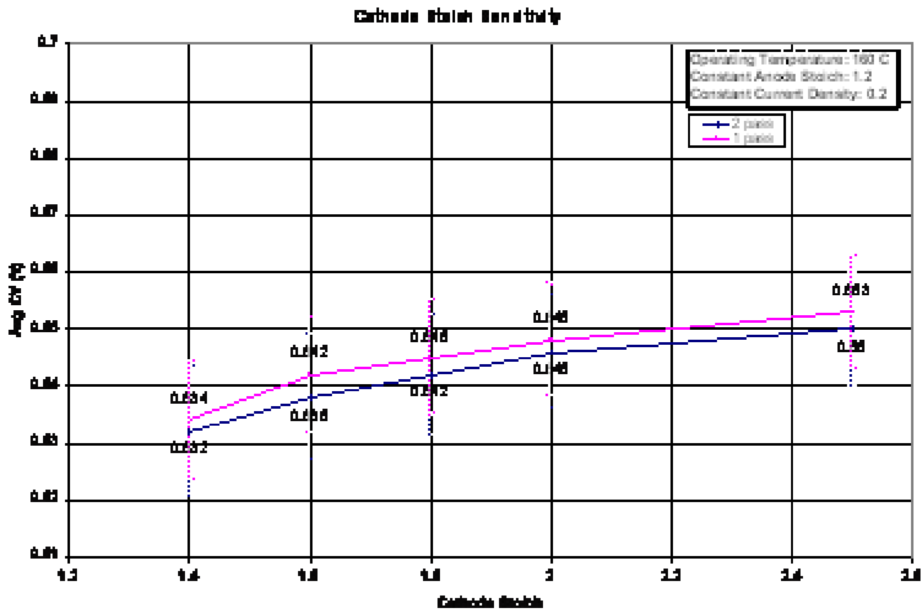

Figure 12: H_2 Cathode Stoich Sensitivity Comparison.

Hydrogen Cathode Stoich Sensitivity: The second part of the fuel utilization characterization is the cathode stoich sensitivity test. Cathode stoich was allowed to vary from 1.4 to 2.5 while the operating temperature was maintained at approximately 160°C. Anode H_2 stoich was set at 1.2 and the current density remained at 0.2 A/cm^2. Compared to anode stoich sensitivity test, cathode stoich reflected a more apparent impact on average cell voltage. There is approximately 20mV difference between 2.5 and 1.4 cathode stoich and 1-pass setup appeared to be more favorable again by approximately 3mV.

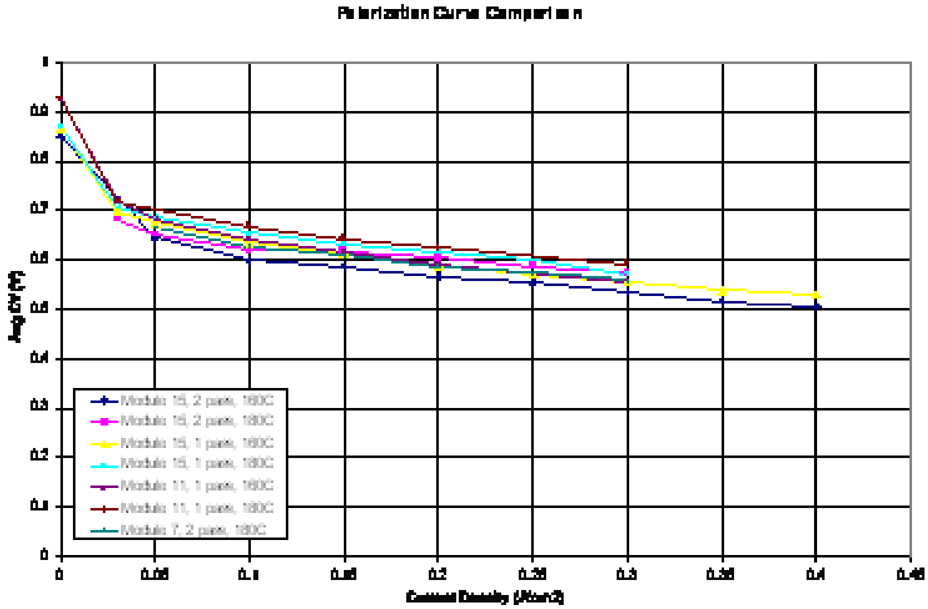

Figure 13: Reformate Polarization Curve Comparison Between Modules 7, 11, and 15.

Reformate Polarization Curve: Three modules were included in the MEA performance comparison: Module 7, Module 11, and Module 15. Module 7 was strictly configured to operate on 2-pass test while Module 11 and 15 was allowed to operate with both anode flow orientations. The most apparent observation of the MEA performance is the average cell voltage production is noticeably better at higher operating temperature.

The difference between the best performed data (Module 11, 1 pass, 180C) and the worst performed data (Module 15, 2 pass, 160C) is approximately 60mV. But no strong connection can be made between MEA performance and anode flow orientation therefore further investigation is required.

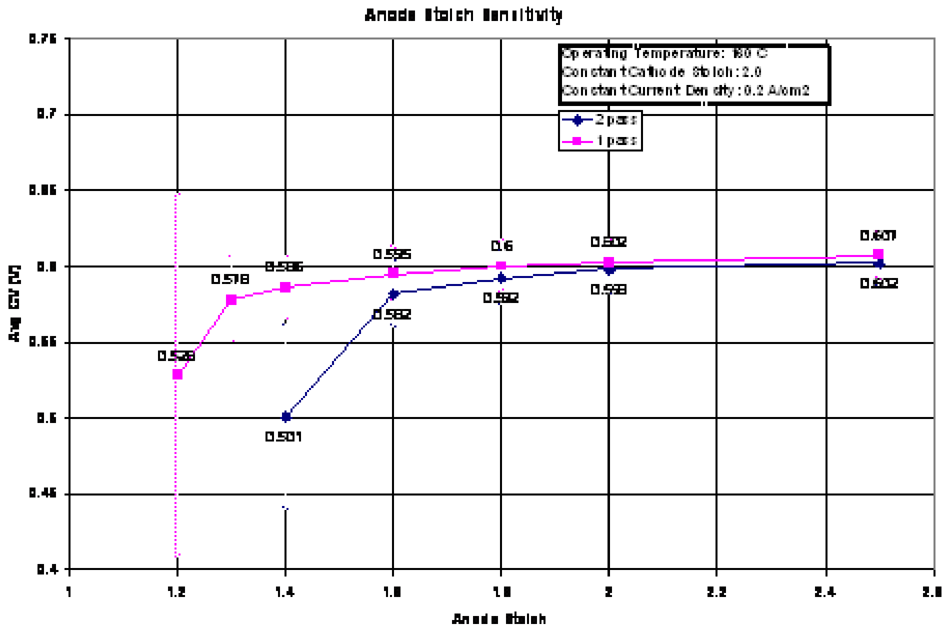

Figure 14: Module 15 Reformate Anode Stoich Sensitivity Comparison Between 1-pass and 2-pass at 160°C.

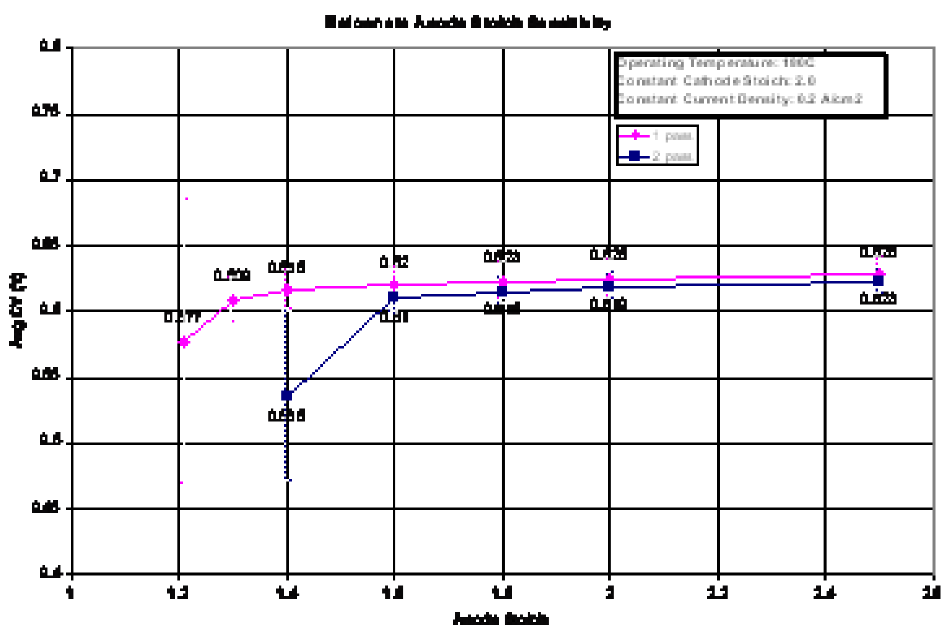

Figure 15: Module 15 Reformate Anode Stoich Sensitivity Comparison Between 1-pass and 2-pass at 180°C.

Reformate Anode Stoich Sensitivity: Two different temperatures were tested for reformate fuel utilization. Both tests were performed with constant operating temperatures, cathode stoich and current loading. The result revealed the effect of operating temperature on cell voltage production. At higher operating temperature, the average cell voltage production is higher. Comparing Figures 14 and 15, with a 20°C elevation in operating temperature, a minimum increment of 20mV cell voltage was observed at each stoich setting.

At 160°C operating temperature, anode stoich impact begins to be more observable when operating below 1.8 stoich. At 1.8 anode stoich, the difference between 1-pass and 2-pass was about 13mV and at 1.4 anode stoich the difference increased to 80mV.

Also noticed 2-pass anode flow orientation was not able to achieve stable fuel utilization under 1.4/2.0 at 0.2A/cm^2 current loading, while 1-pass anode flow setup was able to achieve a stable cell voltage production at anode stoich as low as 1.2 stoich. This was a very interesting observation because 1.2 anode stoich was not observed in the 2-pass modules built in the past. This result suggested that 1-pass anode flow orientation provide a more efficient MEA fuel utilization.

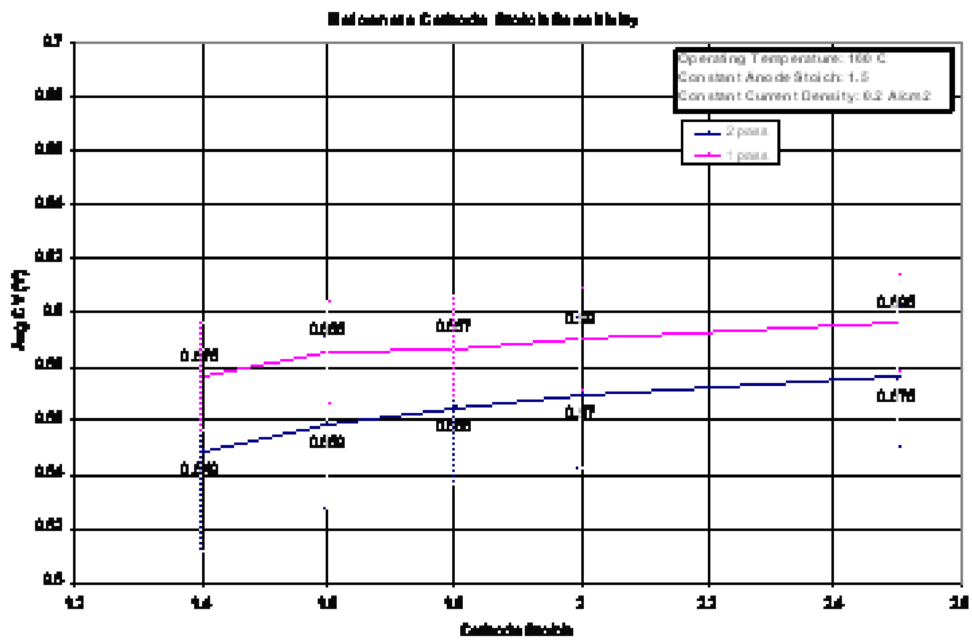

Figure 16: Module 15 Reformate Cathode Stoich Sensitivity Comparison Between 1-pass and 2-pass at 160°C.

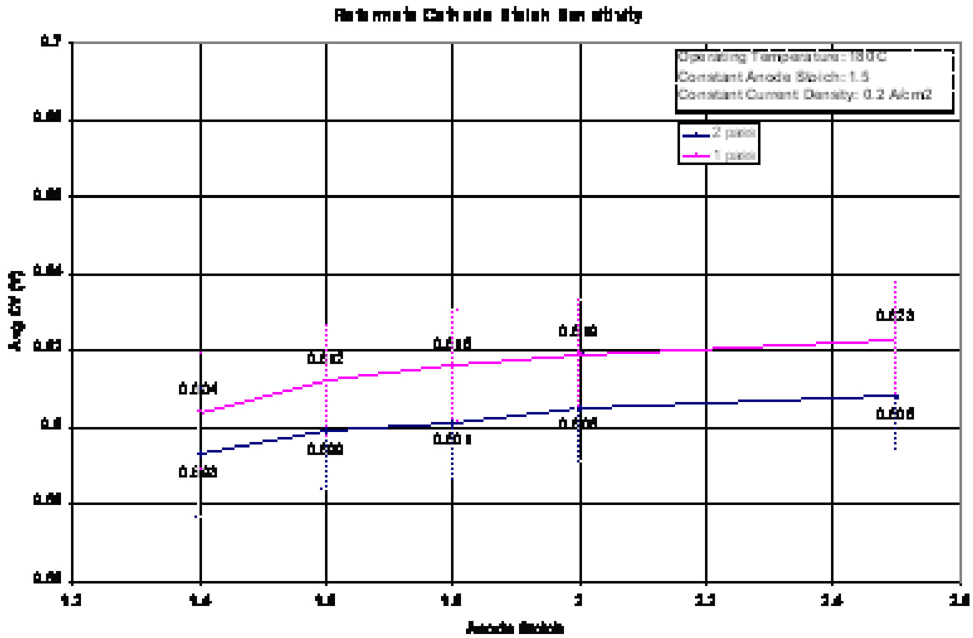

Figure 17: Module 15 Reformate Cathode Stoich Sensitivity Comparison Between 1-pass and 2-pass at 180°C.

Reformate Cathode Stoich Sensitivity: Figures 16 and 17 presents the data recorded during the cathode fuel utilization test. Both tests were performed under constant current density, operating temperature and anode reformate stoich.

Like the anode stoich sensitivity test, there is also an approximate 20mV increment in average cell voltage production with a 20°C elevation in operating temperature. However although the flow direction of cathode reactant gas remained unchanged, the results suggested an approximate 20mV difference between 1-pass and 2-pass anode flow configuration for both 160°C and 180°C. And in both graphs 1-pass appeared to be the more favorable configuration.

The objective of the testing was to perform a BOL test on two different anode flow configurations. The experimental results were recorded and analyzed and all of the results plotted suggested 1-pass as the more favorable configuration for fuel utilization.

It must be noted that a 2-pass anode configuration will, thermodynamically, yield higher stack efficiencies and may be required to get system electrical efficiencies over 40%. This testing concludes only that our current hardware is incapable, from a manufacturing tolerance standpoint, of performing robustly in a 2-pass configuration and that we are pulling back to a more forgiving, more manufacturable design until we understand the phenomena more closely.

Phosphoric Acid Traps

The acid traps used within the power generation module are required to filter out any evaporated phosphoric acid to protect down stream components. The current design uses two different sizes of media to prevent becoming clogged with particulate.

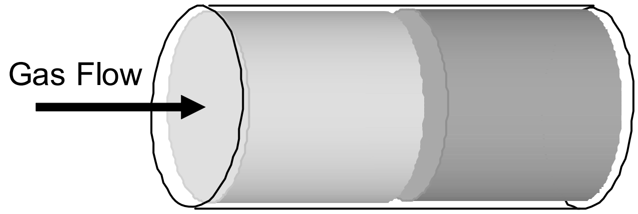

The first section uses a smaller # cells/in^2 filter and the second section uses a larger # cells/in^2 to increase the adsorption of phos-acid species.

A sample was used on a 16-cell module for 8000 hrs and was autopsied to find parameters used to determine the size of the acid trap for system use.

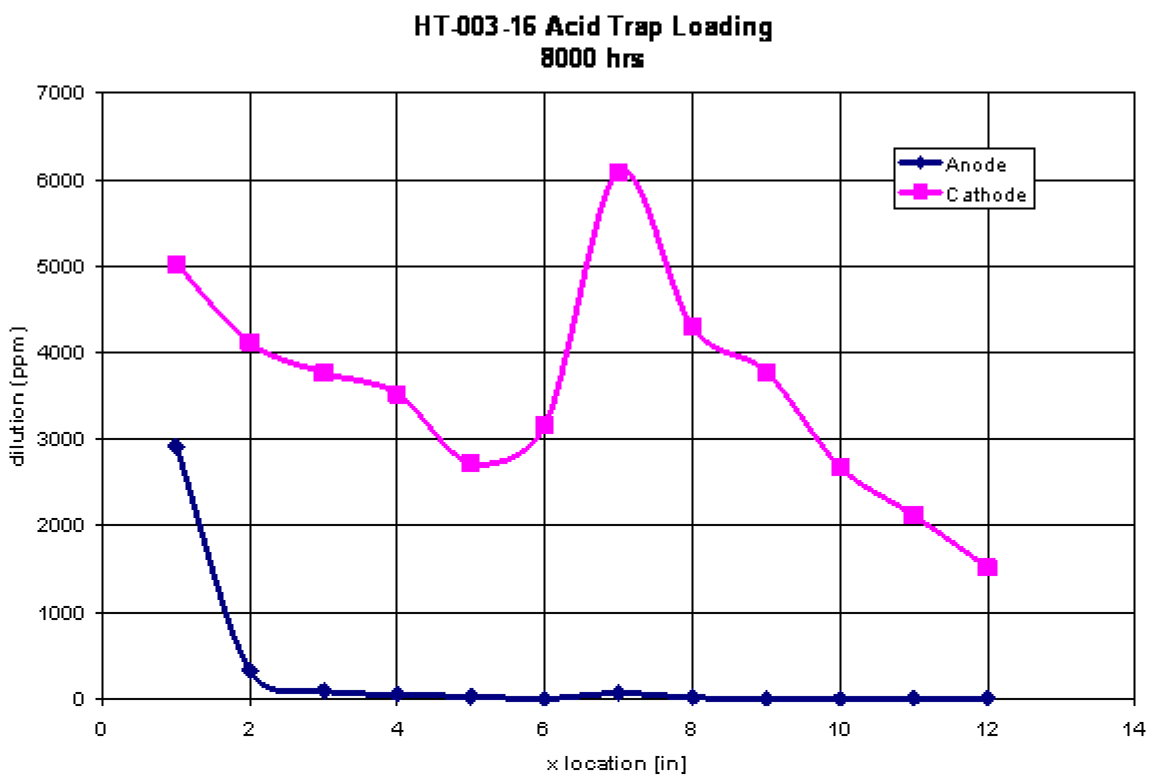

Figure 18: HT-003-16 Acid Trap Loading

The data collected shows that the anode acid trap is oversized and could be reduced to include only ~50% of the small filter and ~15-20% of the larger for ~ 1 year of operation. The data collected for the cathode shows that the acid trap has broken through allowing phos-acid species to leak into the system. This break-through prevents high confidence design data from being attained to properly design the acid trap for system operation as the point of 0 concentration is of particular interest. Linear extrapolation was discussed;

however, higher confidence design data is needed for the design of this component. Therefore, a second acid trap was removed from actual system operation at 5500 hrs in an attempt to gain better insight into acid trap design for the cathode side of the stack.

The results of the autopsy showed similar acid concentrations between anode and cathode traps with the concentrations never settling to zero over the length of the trap. This means that in our current configuration there definitely is phosphoric acid breakthrough in the traps to the rest of the system, specifically the reformer. An ongoing question will be what concentrations of acid the downstream equipment can see without unacceptable degradation. The next generation of acid traps will be fitted with sample ports at the outlets so we can determine the concentrations in the streams.

Figure 18 shows acid concentrations as a function of position along the trap. Note the small spike in concentration after position six as the streams exit the coarse trap and enter the much finer trap.

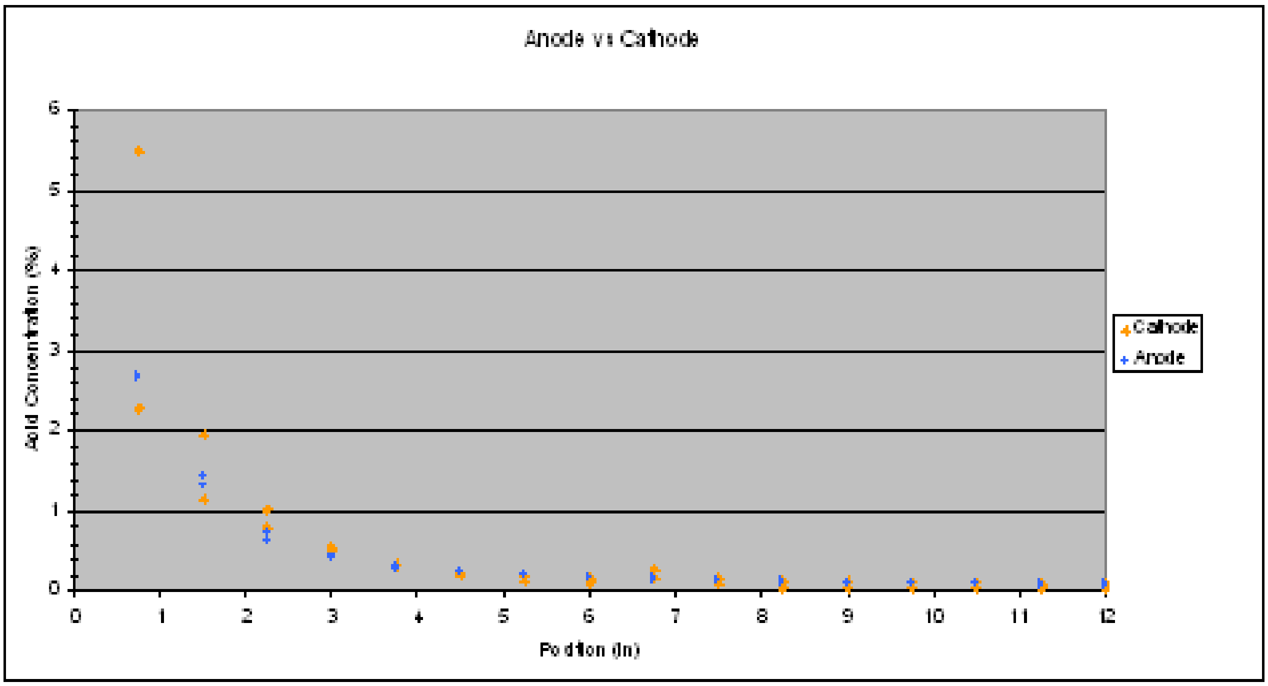

Figure 19: Acid Concentration as a Function of Position in Acid Trap

End Hardware and Assembly

Over the course of the program an ongoing activity has been to take height measurements of assembled stacks between the top and bottom end plates. This is done to provide an indication of stack compression and how it is affected by creep and stress relaxation once pressure is applied. The study has provided significant data that is used to determine when the stack has reached its "hard-stop," assuring that the designed MEA compression has been reached. Along with its intended purpose the data collected has shown some unexpected variations in the distance between the end plates during load application. This brought up the issue of end hardware deflection in terms of its magnitude and affects on the compression of the stack. A finite element analysis was done to approximate the magnitude of the end hardware deflection.

In this scenario centerline symmetry is used to simplify the analysis of the 6061 Aluminum end plate. The stack is assumed to be compressed to 6,000 pounds of force. The following loads and constraints were used: (Figure 20)

- 1,000 lbs at each tie rod location
- 2,500 lbs in the active area portion
- 500 lbs in the gasket groove area
- 0 Y displacement at the center of the part
- 0 Z displacement along the Z-axis of the part
- 0 X displacement along X-axis of the part

This scenario uses simplifying assumptions to simulate the actual load state. Some of these assumptions include:

- Equal tension placed on all tie rods
- Identical spring constants for each tie rod
- Even load distribution across active area and gasket area sections
- Thermal expansion not taken into account

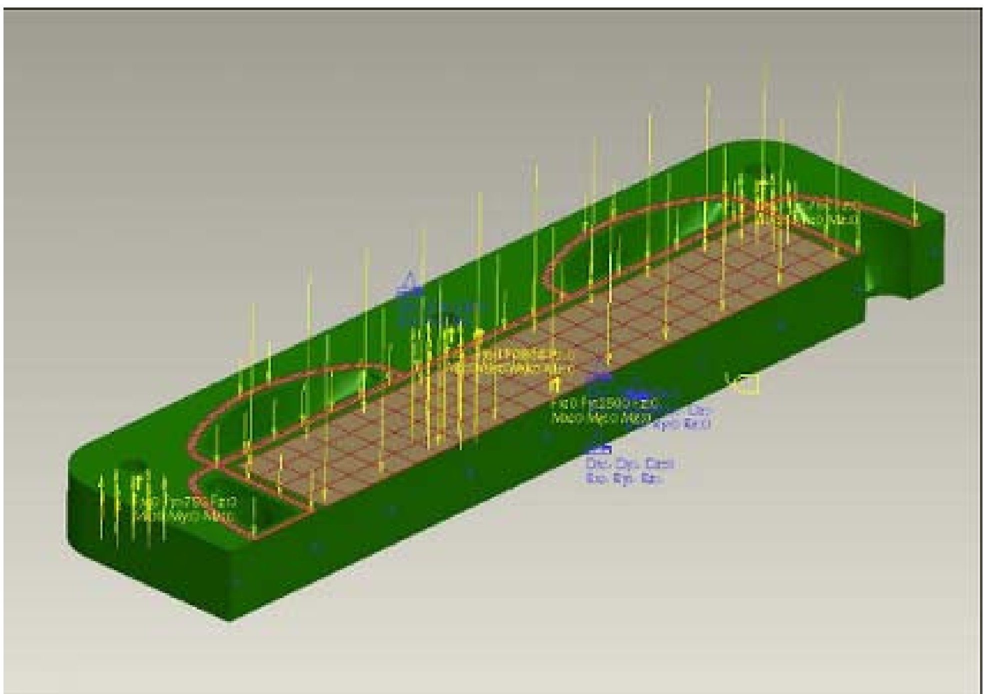

Figure 20: Stack End Plate FEA

Figure 21 below shows the Y-displacement plot of the analysis.

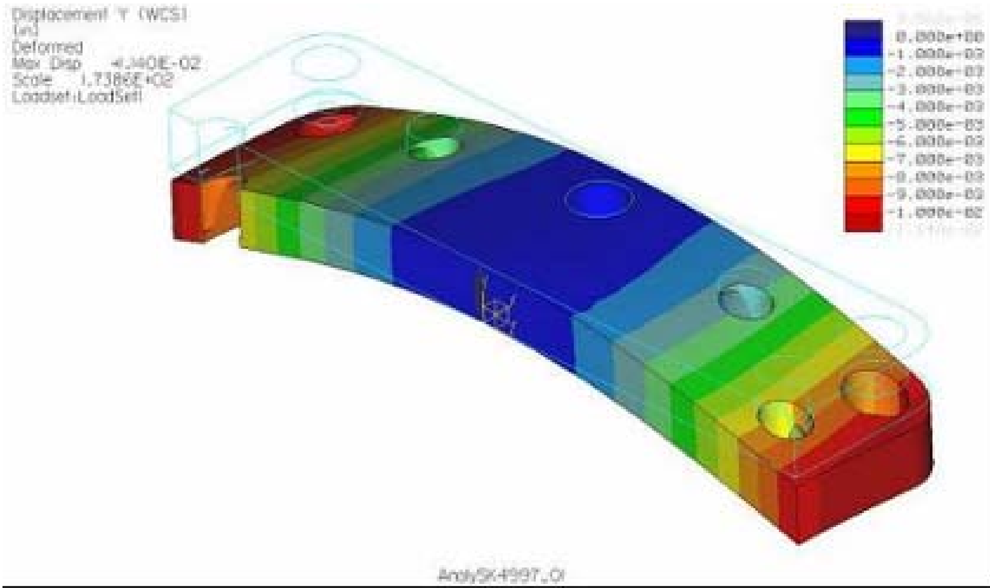

Figure 21: Stack End Plate Deflection

The maximum displacement of the part is approximately .011", occurring at the far corners of the part. Further analysis shows that the Y-displacement along the active area centerline is closer to .006". Assuming that this deflection affects the top 20 cells in the stack it would result in .0003" of deflection taken from each cell. This would move the nominal cell compression from 21.6% to 20.8%.

To minimize the end hardware in the future it is possible to make the 1.5 thick end hardware even thicker. Another possibility would be to use stiffer springs on the four tie rods at the corners. This study will be used in conjunction with future work to dictate the future design of the stack end hardware.

Two stacks were built and analyzed to study compression of the MEA. MEA compression distribution charts are summarized below.

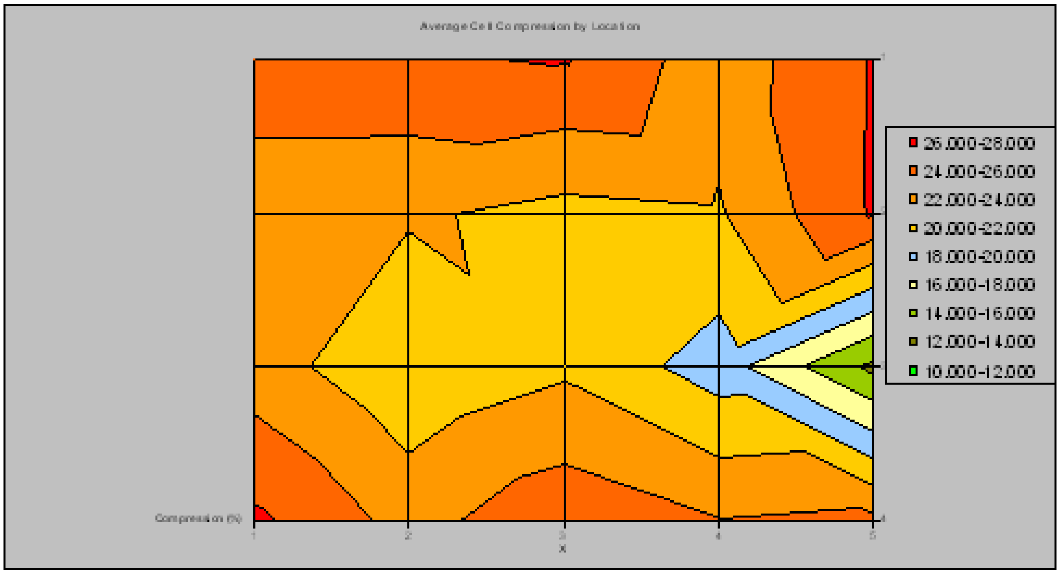

Figure 22: HT-022-80 MEA compression distribution

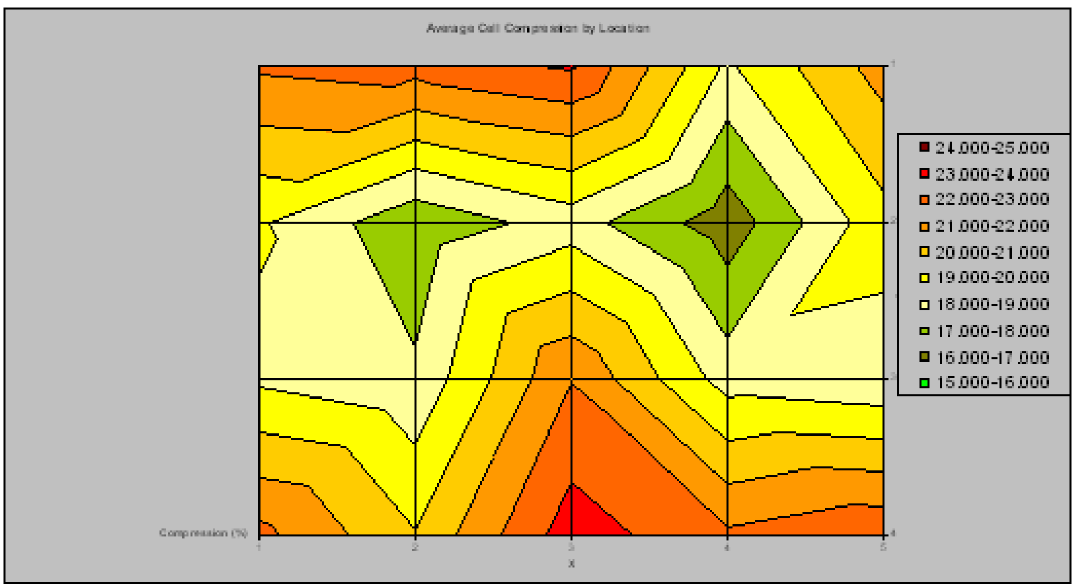

Figure 23: Average Cell Compression HT-026-80

In module 22, five cells show no contact in the lower right edge due to a deep pocket on the bipolar plate. In 26, several cells show undercompression in the flowfield area. These issues have been resolved by our vendor and we have determined root cause and corrective actions. We are continuing to track performance of these cells to determine impact on performance over life.

High Temperature Molded Plate

Several new materials were evaluated for use in high temperature plates. A thermoplastic based plate material as well as a thermosetting material was evaluated. Improvements in material integrity and thus plate robustness as well as cost are the driver for new plate materials.

Overview: Compression molding offers the potential to reduce manufacturing costs far below what machined plates are capable of. Pacific Fuel Cell Corporation (PFC) was the original partner on this project but the development program dissolved after a careful review of new design's requirements. As of the end of this program, new plate development partners were being evaluated. PFC produced the first samples of plates and assisted in debugging the process at their manufacturing facility in Willoughby, OH. Four mold tools that fit a PFC compression mold machine and a mold pre-form owned by Plug Power were provided for the process. Employees at PFC have previously worked on compression molding HT plates.

The first batch of molded plates was received from PFC. This batch consisted of 40 plates in total which were divided into groups of 10 based on processing conditions. The conditions were: no post-bake no de-flash, no post-bake de-flash, post-bake no de-flash, post-bake and de-flash. A batch of old plates was also run through the measurements for comparison. Per the test and verification plan these plates were first run through a series of dimensional checks using an OGP as well as contact probe measurements. Some of the findings from these dimensional analyses can be found in the charts and tables below.

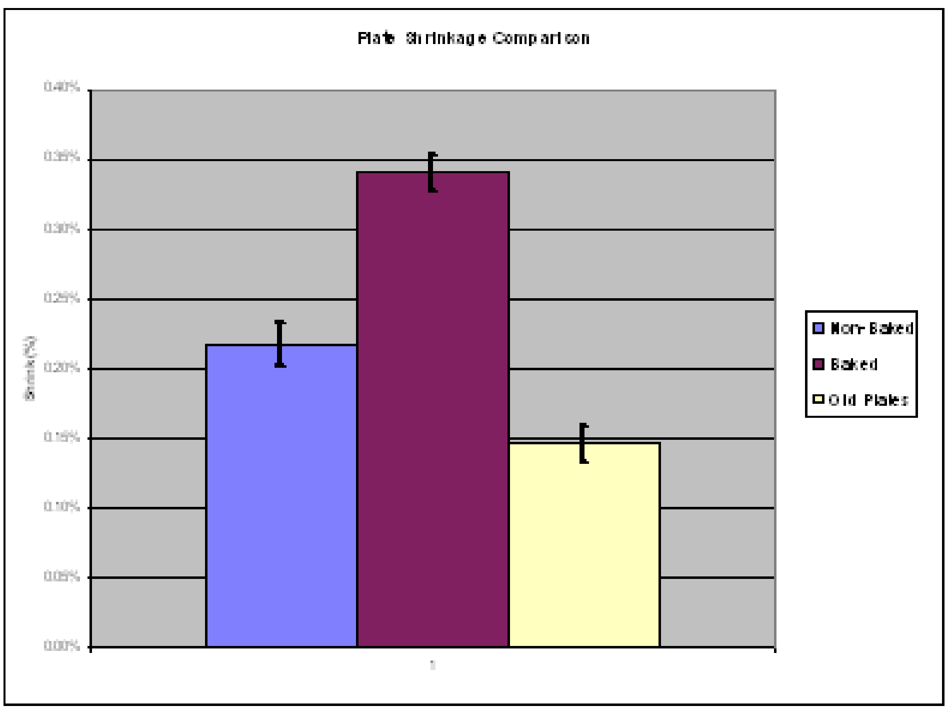

Figure 24: Stack Plate Shrinkage Analysis

Figure 24 shows that the final shrink of this plate batch for finished (post-baked) parts came in at .34%. Shrinkage out of the mold accounts for about 65% of this total shrink while post-baking accounts for the rest. An interesting find was that the older plates (believed to be post-baked) show only 44% of the shrink compared with the newer post-baked plates. If the plates were not post-baked then it is possible that the 2σ error bars would overlap with that of the non-baked plates (error bars shown represent (1σ). The older plates represent a different supplier's process from more than a year ago. If they were in fact post-baked it is important to gain knowledge of the process parameters which caused the extra shrinkage of the newer plates.

Shrink Summary				
Condition	**Average X Shrink**	**X STDev**	**Average Y Shrink**	**Y STDev**
Non-Baked	0.22%	0.015%	0.21%	0.013%
Baked	0.34%	0.013%	0.31%	0.060%
Old Plates	0.15%	0.013%	0.15%	0.022%

Figure 25: Stack Plate Shrinkage Summary

Figure 25 breaks the nominal shrinkage values into X and Y components. This is useful in that it shows that for all three species the shrinkage in the X and Y directions is almost identical. Different values in X and Y would have created a more complex situation for the plate design and manufacturing process.

Z dimensions taken on the OGP provided data that showed a great deal of variation in hard-stop height, gasket groove depth, and MEA pocket depth. Since the depth measurements utilize the hard-stop as a reference plane it was impossible to extrapolate how each feature is varying in relation to another. For this reason contact measurements were used to determine the thickness of each feature at several points on the plates. Figure 26 below shows the measurement locations. (different colors denote different measurement planes).

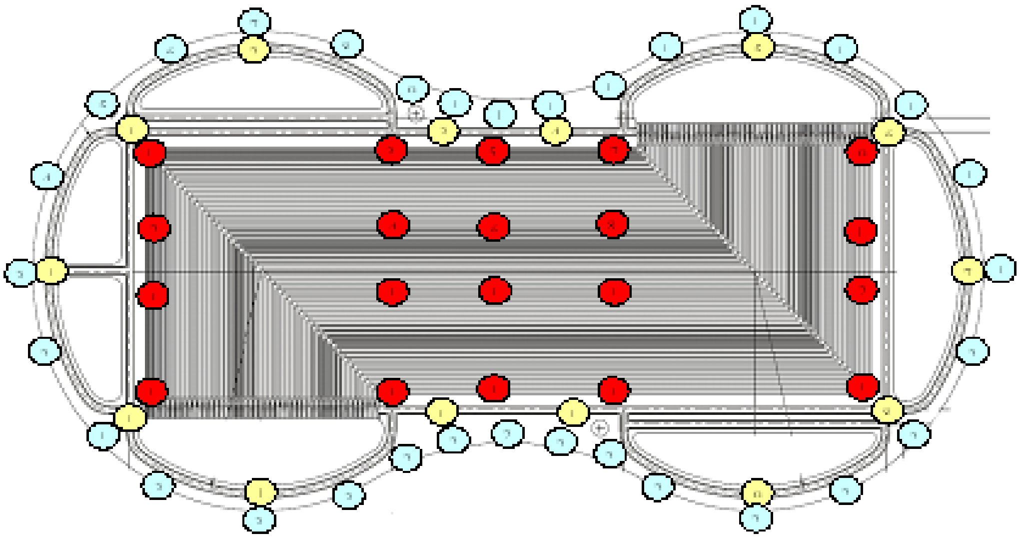

Figure 26: Stack Plate Shrinkage Measurement Locations

The results for the non post-baked plates can be seen below in Figure 27.

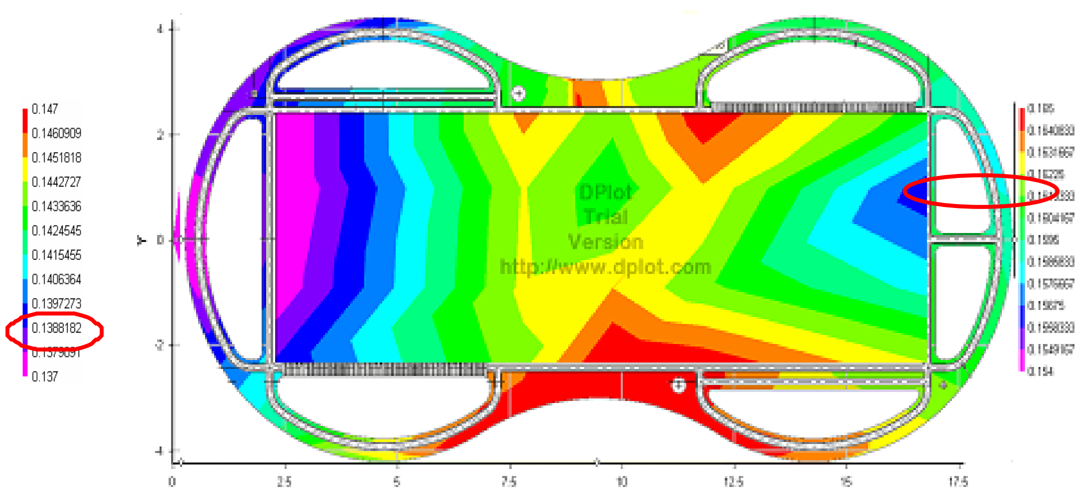

Figure 27: Non Post-Baked Plate Thickness Distribution

Two different scales are used on this plot of thickness. The hard-stop or outer portion of the plate uses the scale on the right side of the image. The MEA pocket thickness uses the scale on the left side of the image. In each case the expected nominal thickness value has been circled in red.

Figure 28 below shows the same type of output for the post-baked plates.

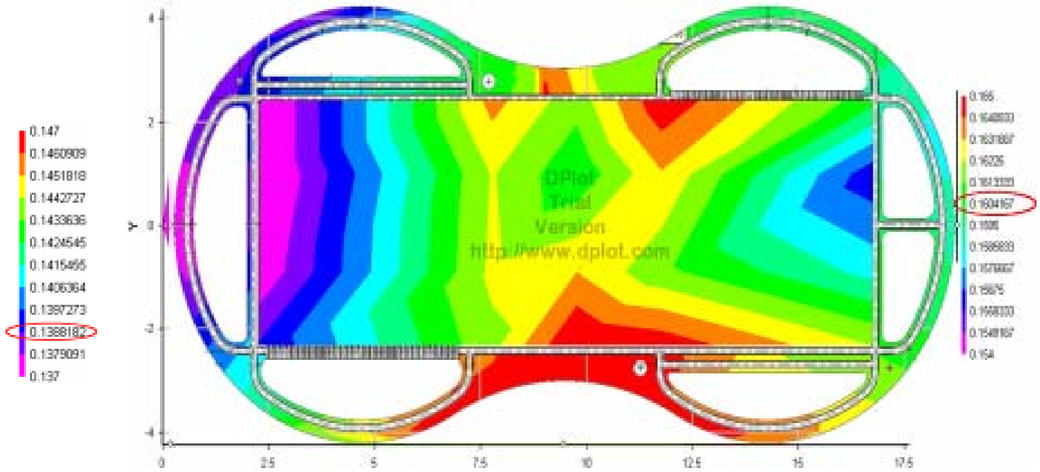

Figure 28: Post-Baked Plate Thickness Distribution

It can be seen in both of these images that the thickness is greatest in the middle of the plate and then drops off as you move to the left or right. This gradient is consistent across both of the planes shown in these images. The variation is approximately 0.010" for both planes in both baked and non-baked states. Thickness control in the z-plane is clearly something that needs to be controlled better moving forward. Process parameters that could have an affect on this include: pre-form design, pre-form placement, material flowability, and closing speed of the mold.

In 3Q08 the team decided that based on the combination of our current vendor's raw material, molding process and plate design a molded initiative at this time is not feasible and work on this initiative is complete for this program. Future plans include reviewing commercially available materials and seeking new suppliers with more sophisticated molding experience.

Chemical and moldability tests have been initiated with three different raw material samples. The results of these tests will be used to determine which material is believed to behave the best from a manufacturability as well as durability stand-point. The earlier phases of this project are scheduled to be complete H209. The initial tool design and fabrication is expected to be complete H209 with prospects of a molded stack as early as Q409.

Silkscreen Insulator Height Study

It is currently understood that for optimum MEA performance in the high temp stack, a nominal cell compression of 20% +/- 5% must be maintained (per BASF's recommendations). The stack components that determine cell compression are plate pocket depth, mea thickness, and Viton insulator height. To calculate this value the following compression formula is used:

*[MEA – (IH + PD)]/MEA * 100 = Cell Compression (%)*

MEA = MEA Thickness

IH = Insulator Height

PD = Pocket Depth

The assigned nominal values and associated tolerances of these components must work together to keep the mea compression within the allowable range (15% - 25%). Figure 29 below shows the affects the tolerance of the insulator height, by itself can have on MEA compression.

		Table 1
Allowable Tolerance	**Lower Compression Limit (%)**	**Upper Compression Limit (%)**
0	21.62	21.62
0.0005	20.27	22.97
0.001	18.92	24.32
0.002	16.22	27.03
0.003	13.51	29.73
0.004	10.81	32.43

Figure 29: Insulator Thickness Tolerance Effect on MEA Compression

If the insulator was the only component to vary it would begin to cause compression problems at a tolerance of +/- .002”. However, since the pocket depth and MEA thickness also have an associated tolerance (with approximately the same affects on compression), it is necessary that the insulator height be kept at an even tighter tolerance.

It is current practice to measure all of these compression dimensions, for 16 cells on each stack build. Typically, 12 points on each cell insulator have measurement heights taken. For the purpose of this test 24 points were used to gain better resolution. 12 bi-polar insulators and 10 anode coolers were measured, all of which were received in the latest order of plates and insulators. Figure 30 below indicates the locations of measurements. Red denotes locations typically measured in stack builds while the yellow locations were added for this test.

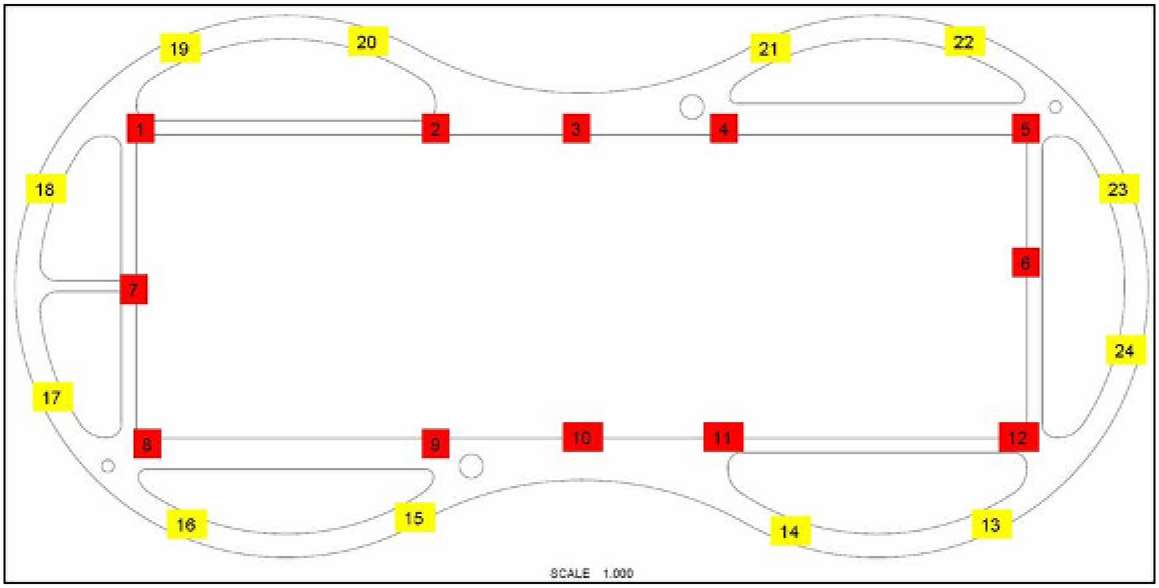

Figure 30: Silkscreen Thickness Measurement Locations

The average values for each type of plate as well as the overall average can be found below in Figure 31. The table has been formatted so that numbers above the spec. are highlighted red while numbers below the spec. are in green. The conditions used were .008" +/- .001".

Table 3

Average Heights			
Location	Bi-Polar (in)	Anode Cooler (in)	Overall Height (in)
1	0.0072	0.0081	0.0076
2	0.0072	0.0074	0.0073
3	0.0062	0.0069	0.0065
4	0.0062	0.0075	0.0068
5	0.0063	0.0077	0.0069
6	0.0077	0.0084	0.0080
7	0.0068	0.0077	0.0072
8	0.0064	0.0079	0.0071
9	0.0067	0.0071	0.0068
10	0.0060	0.0074	0.0067
11	0.0069	0.0076	0.0072
12	0.0075	0.0087	0.0080
13	0.0064	0.0088	0.0075
14	0.0067	0.0091	0.0078
15	0.0065	0.0088	0.0075
16	0.0071	0.0088	0.0079
17	0.0069	0.0084	0.0075
18	0.0070	0.0081	0.0075
19	0.0067	0.0080	0.0073
20	0.0068	0.0082	0.0075
21	0.0067	0.0080	0.0073
22	0.0068	0.0084	0.0075
23	0.0068	0.0085	0.0075
24	0.0071	0.0100	0.0084
Average	0.0068	0.0081	0.0074

Figure 31: Summary of Average Silkscreen Thickness Measurements

The bi-polar plates were on average lower than specification at most of the measurement locations with the average coming in at .0068”. The anode coolers were in specification at most locations with the .01” value at location 24 standing out as an outlier. There is clearly a difference between the insulator applications on the batch of bi-polars vs. the anode coolers. Figure 32 below shows the variation in the height at each location by looking at the value of 2 standard deviations (95% confidence). The formatting in this chart highlights any values greater than .002” in red. It can be seen that high variations exist for both plates at locations 3, 10, and 11. In general the anode coolers appear to be in less control than the bi-polars.

Table 4

2 σ			
Location	Bi-Polar (in)	Anode Cooler (in)	Overall (in)
1	0.0010	0.0016	0.0013
2	0.0012	0.0017	0.0014
3	0.0028	0.0022	0.0025
4	0.0017	0.0019	0.0018
5	0.0016	0.0030	0.0023
6	0.0019	0.0013	0.0016
7	0.0016	0.0021	0.0019
8	0.0012	0.0026	0.0019
9	0.0009	0.0021	0.0020
10	0.0020	0.0034	0.0027
11	0.0030	0.0027	0.0024
12	0.0012	0.0049	0.0030
13	0.0009	0.0024	0.0016
14	0.0016	0.0032	0.0024
15	0.0010	0.0023	0.0017
16	0.0016	0.0035	0.0026
17	0.0010	0.0020	0.0015
18	0.0010	0.0011	0.0011
19	0.0014	0.0009	0.0011
20	0.0014	0.0012	0.0013
21	0.0012	0.0008	0.0010
22	0.0017	0.0014	0.0016
23	0.0017	0.0020	0.0019
24	0.0016	0.0055	0.0036
Average	0.0015	0.0023	0.0019

Figure 32: Statistical Distribution of Silkscreen Thickness by Plate Type

Figures 33 and 34 below serve as a useful tool in determining what the shortcomings of each batch are. To reiterate, the bipolars are shifted off the target and have too wide a distribution. The anode coolers are centered well on the target but have an even wider distribution.

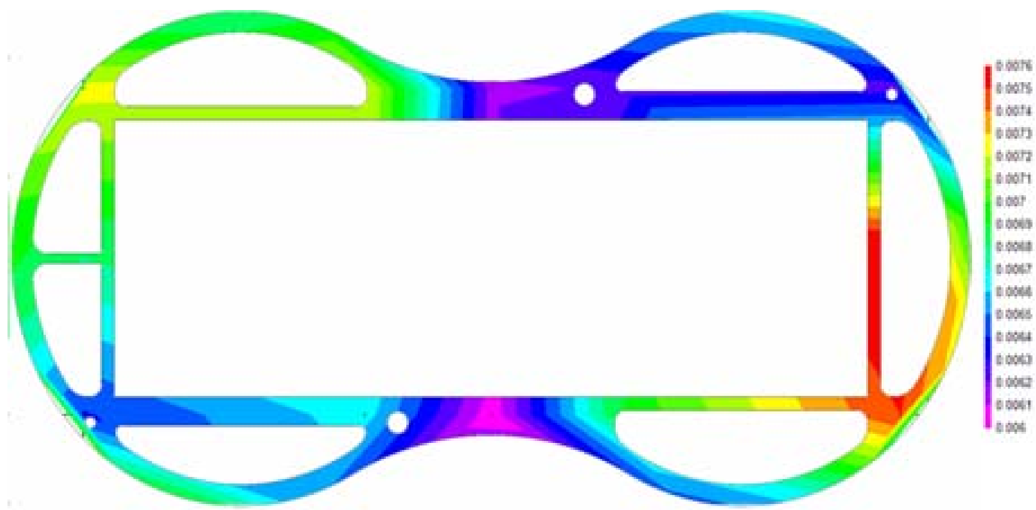

Figure 33: Bipolar Plate Silkscreen Thickness Distribution

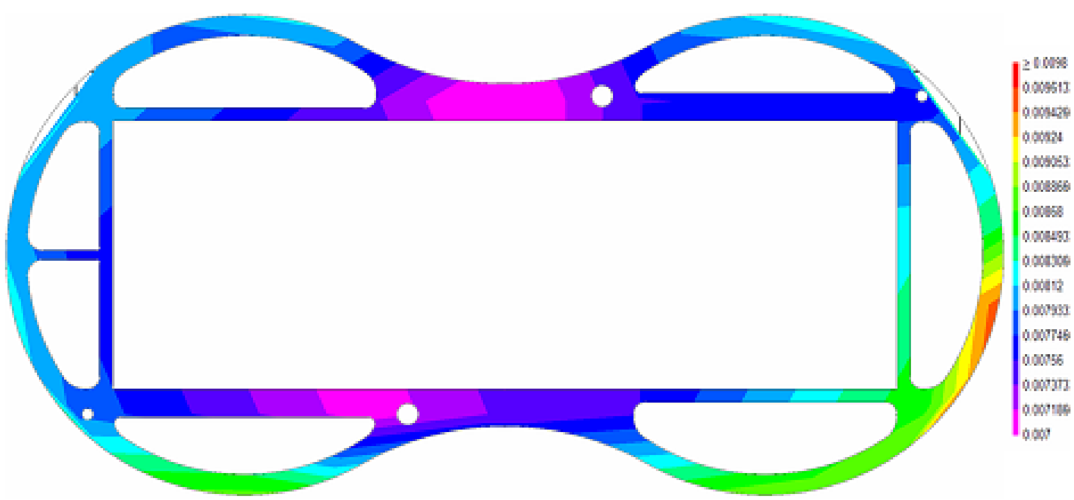

Figure 34: Anode Cooler Plate Silkscreen Thickness Distribution

Please note that the scales for these two charts differ as the nominal and range of the anode cooler measurements were both larger than that of the bi-polar. It does appear that in both cases the center portion of the plate (measurements 2-4 and 9-11) are lower than the ends of their respective plates.

The results of this study are being shared with the supplier in order to leverage work towards improving the nominal and distribution of the insulator height.

Long-Term Stack Testing
Three stacks underwent long-term testing and evaluation during this program: HT-019-16, HT-022-80, and HT-023-16.

HT-22-80
This stack was broken in and characterized IAW HT-070006 Rev C, Break in and Characterization, with the following exceptions:

- The time allowed for break in was reduced to about 60 hours, instead of 100 hours, due to delivery constraints.
- All characterizations were performed using dry gasses, as the test station does not have the ability to humidify gasses.

Break in was performed at 1.2/2.0 stoich on pure H2 at 0.2A/cm^2. The plots below show the voltage, temperature, and pressure profiles. Gap between hours 20 and 30 was a shutdown to replace the coolant flow meter, which had failed.

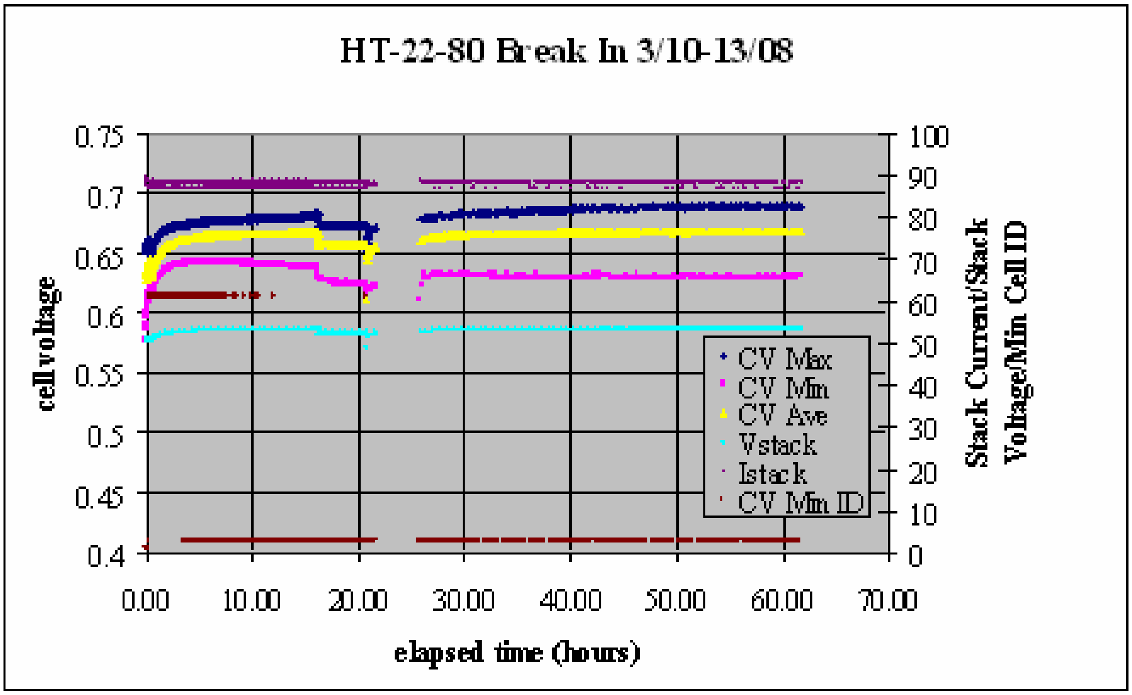

Figure 35: Break In Voltage

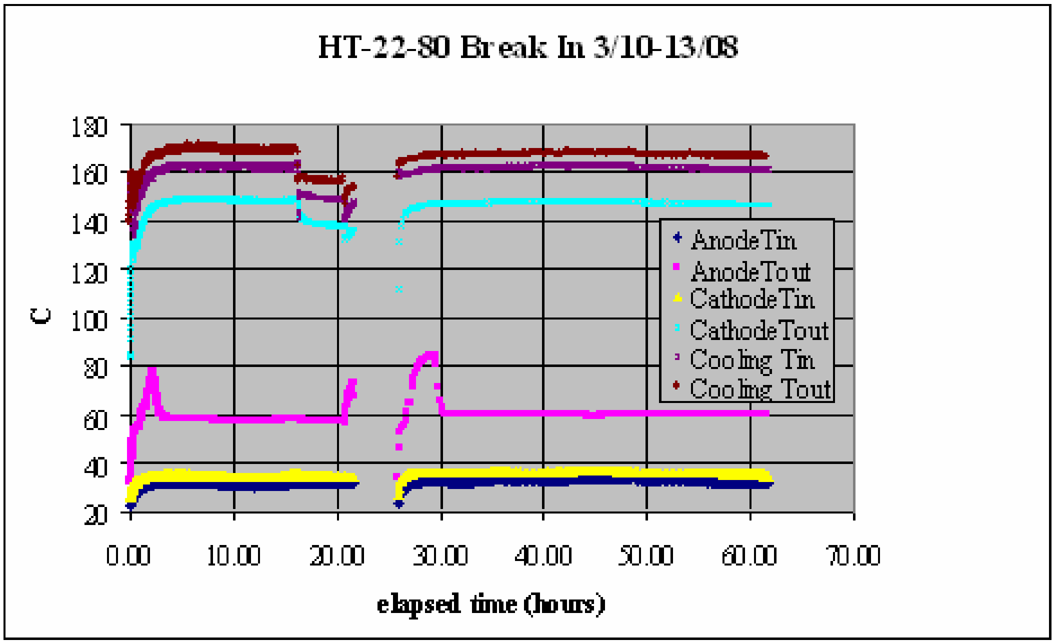

Figure 36: Break In Temperatures

Characterization was performed IAW HT-070006 Rev C, which included H2 constant stoich and stoich sensitivity tests, followed by reformate constant stoich and stoich sensitivity tests. Hydrogen testing was performed at 160C. Reformate testing was performed at both 160 and 180C. Reformate blend D was used, which has 29% H_2, 9% CO_2, 1% CO and balance N_2. All testing was performed with dry gasses. Figures below detail the results obtained. Error bars indicate +/- 2 stdev.

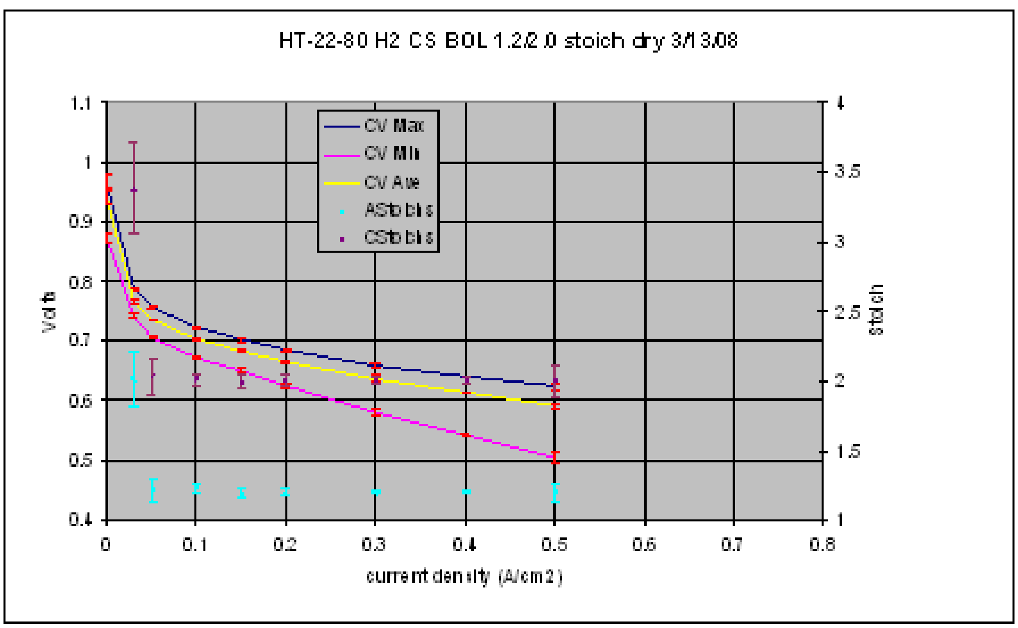

Figure 37: H2 Constant Stoich Test

The stack appeared capable of operating at 0.6A/cm^2 on H_2, however the load banks were unable to dissipate sufficient heat for operation at this current level. Additionally, coolant differential temperature was 17C(160C supply), coolant supply pressure was 3.5 PSIG and coolant flow was 2.5 GPM, indicating shortcomings in the heat removal capability of the stack.

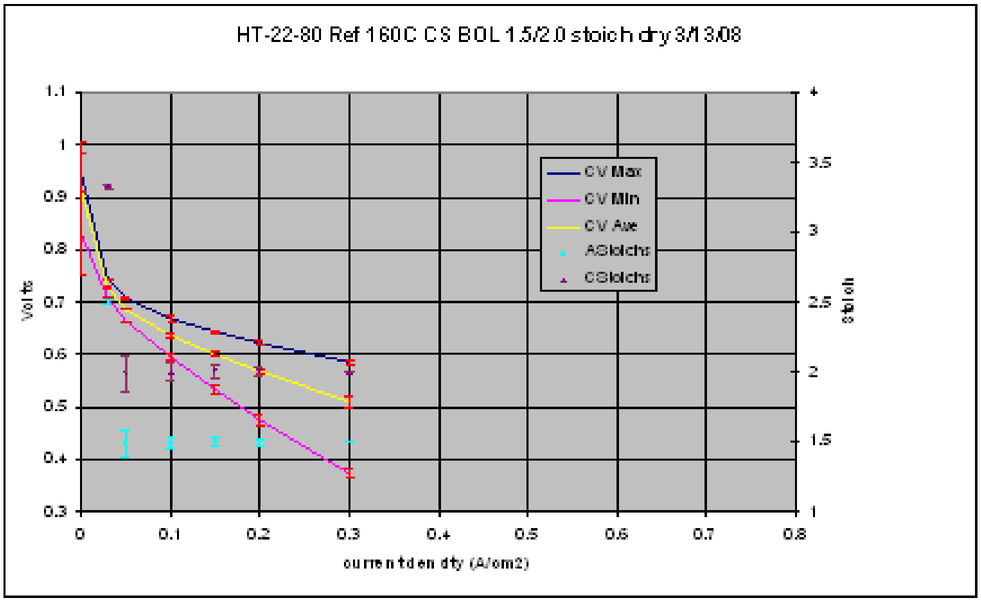

Figure 38: Reformate Constant Stoich Test at 160C

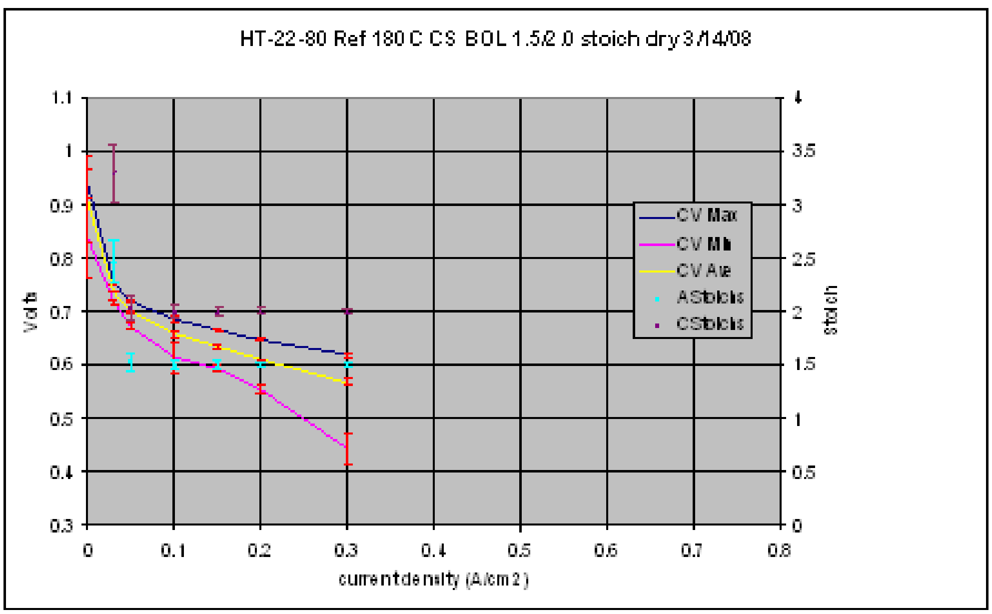

Figure 39: Reformate Constant Stoich Test at 180C

In conclusion, HT-022-80 incubated well. Its BOL characterization test showed high anode stoich sensitivity on reformate and not on H_2 which indicates an electrode issue or an unexpected CO sensitivity. This issue has been communicated to our MEA supplier and root cause is being sought. HT-022-80 also showed a shift in cell voltage standard deviation between batches of MEA's. This shift was not expected and was also communicated to our MEA vendor for root cause determination.

HT-023-16

The objective of this testing was to measure performance data during the BOL of HT-023-16. The performance data include: Polarization Curve (both H_2 and Reformate D gas), H_2 Stoich Sensitivity at 160°C, Dry Reformate Stoich Sensitivity at 160°C and 180°C, and also temperature impact on standard performance. HT-023-16 was built on March 19, 2008 to test the performance of P2000 MEAs. It consists of 16 cells with active area of 440cm^2, with the end hardware set up for single pass anode gas flow orientation. Both the reactant gases and coolant were introduced in co-flow orientation. The module was installed in Station 8 in Lab 10 which uses steam injection humidification method, however due to hardware failure HT-023-16 was not humidified during BOL.

Standard incubation procedure was followed at 1.2/2.0 stoich on pure H_2 at 0.2A/cm^2. Figure 40 showed the average cell voltage distribution within the first 100 hours of incubation. Three additional Modules (HT-015-16, HT-017-16, and HT-019-16) were included for comparison purpose. Among the 4 modules HT-15 was the only module that used P1000 MEA and all 4 modules were set up for single pass test. Noticed HT-023 has an overall better performance (0.669 V at 80th hour). Another interesting finding was that although the manufacturer recommended a 100 hour MEA break-in requirement, the average cell voltage reached 95% completion at the 80th hour, suggesting a possibility of reducing incubation length by a day.

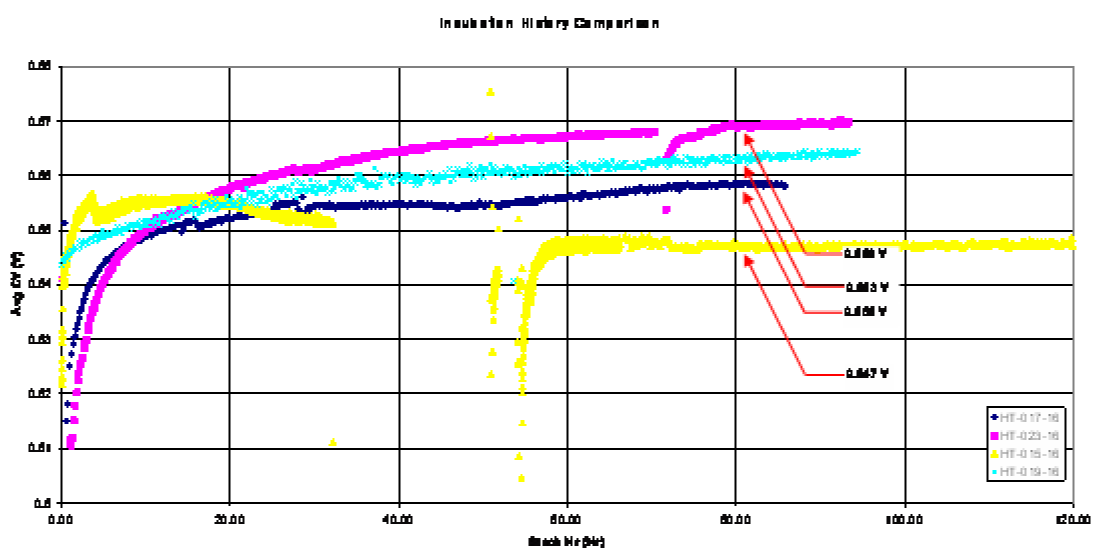

Figure 40: Average CV distribution during incubation

H_2 Polarization Curve: After incubation, a H_2 polarization curve was carried out and the performance data is showed in Figure 41.

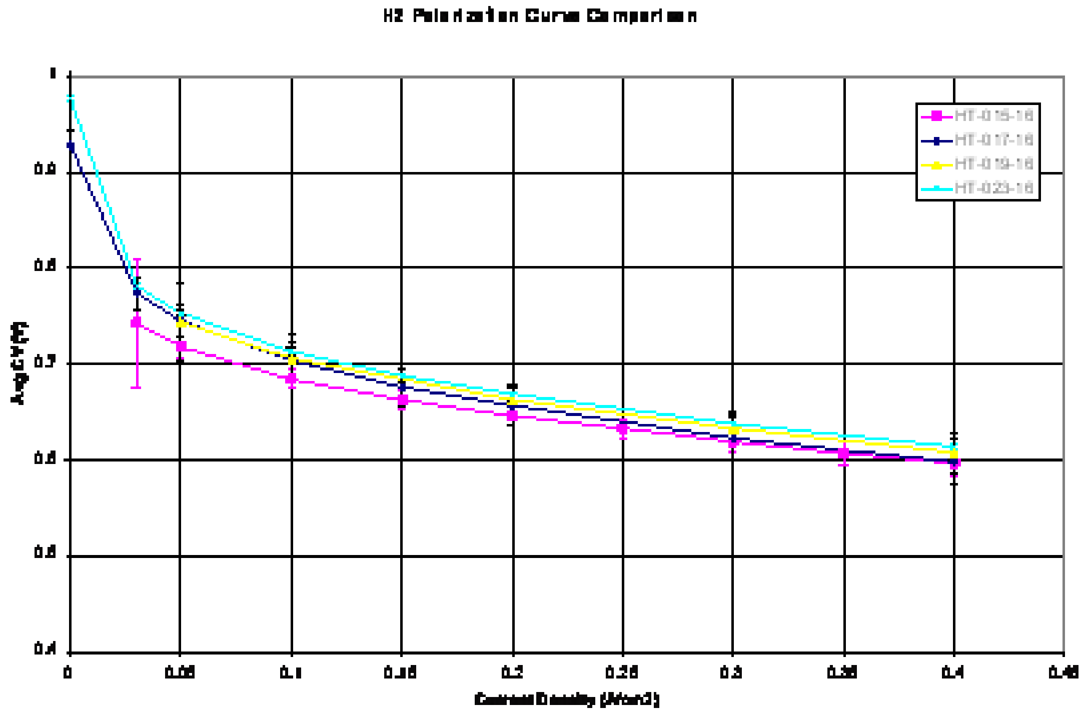

Figure 41: H_2 Polarization curve comparison

The polarization curve showed similar performance between the 4 modules, unfortunately due to hardware limitation, OCV test data were not collected for HT-019 and HT-015. Taking a closer look at the data, HT-023 has a slightly better performance than the other three modules, and a 20mV overall advantage over the P1000 MEAs. The operating temperature during the polarization curve generation were kept constant at 160°C and flow rate at approximately 1 GPM with an exception to HT-017 which was tested on Station #7. HT-017 produced a slightly lower voltage distribution due to questionable coolant flow meter which may result in higher coolant flow rate hence a different coolant inlet and outlet temperature difference compared to other modules.

Ref Polarization Curve: Figure 42 shows the polarization curve of HT-023-16 when operated with Reformate D gas. The results were compared to P1000 HT-015-16 and the plot showed similar behavior in performance between P1000 and P2000 MEAs. Noticed HT-023 was tested on Module Station 8 which were limited by mass flow controller therefore higher current densities were not tested.

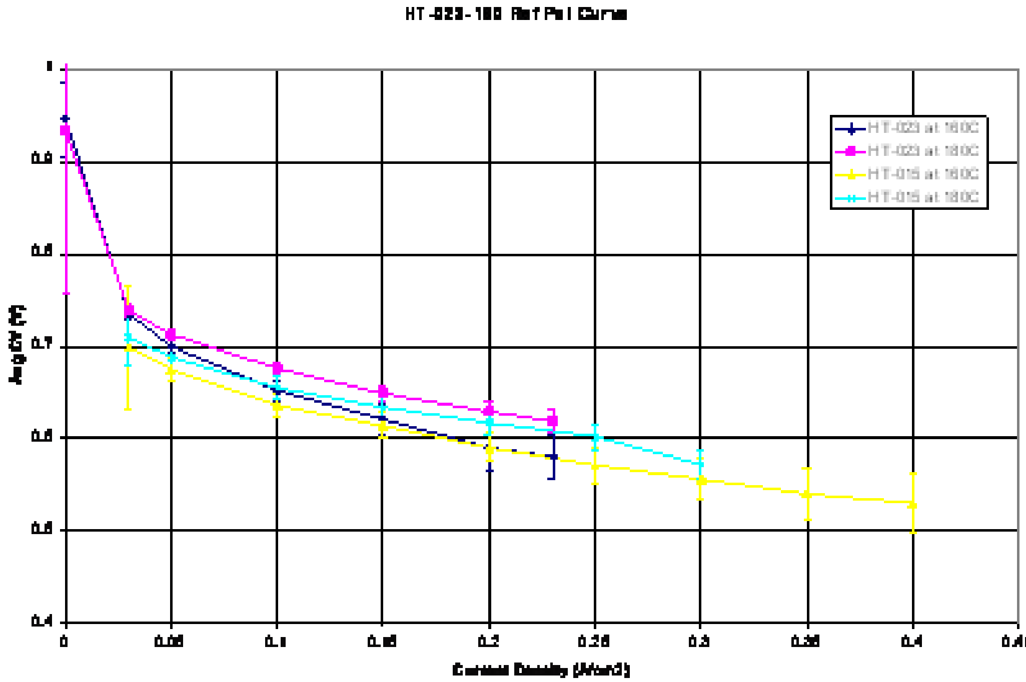

Figure 42: Reformate D polarization curve comparison

HT-023-16 successfully completed the assigned BOL tasks. Due to hardware failure the tests were carried out non-humidified. Some selected results were compared to P1000 MEAs to observe the performance difference between the two batches of MEAs; there is no significant difference on polarization curve performance between the two MEAs, however P2000 has a slight advantage over the P1000 MEAs on electrode performance. On both reformate and air stoichiometry tests, HT-023-16 continued to show the high anode stoich sensitivity as seen on HT-022-80.

Long-term stack testing during this program yielded important data in our understanding of the characteristics of the baseline and improved BASF MEAs. In particular, it allowed us to understand the anode variability issues of their scale up activities and provide them with data to enable a root cause determination and fix.

<u>Task 7: Thermal Management Module – Plug Power</u>

Coolant and house water flow requirements were defined as well as house water allowable pressure drop through the FCHA. This allowed for selection of the prime path CHP HX. The prime path coolant and coolant pump were also selected. Coolant selection was based on superior performance relative to alternates in a product search covering 51 coolants and multiple performance parameters. Pump selection was based on endurance and performance data from in house fuel cell systems developed under prior NIST and NYSERDA programs.

Thermal management testing was ongoing through the program in order to harden the system design, prove our component selection, and perform endurance testing. The majority of this testing was been performed on our Thermal Management Test Rig.

During our testing we have been able to determine many things; the size of the house water heat exchanger, lifetime performance of the coolant which we use in our system, and lifetime performance of our selected coolant pump.

One design change that we have found necessary is to try to reduce the temperature of the coolant pump motor. This increases performance and the lifetime of the coolant pump. The tested and adopted approach is the installation of an insulator plate in between the motor and the pump. This forms a thermal break and reduced the thermal conductivity between our coolant and the coolant pump motor.

Figure 43: Thermal Management Test Rig

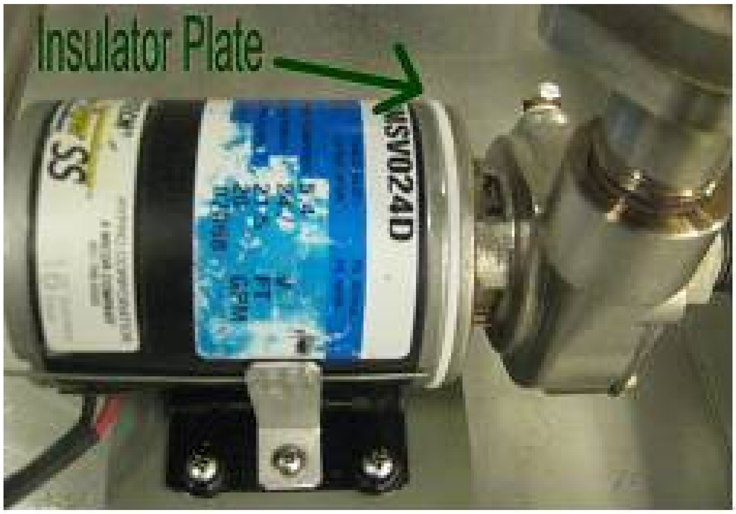

Figure 44: Modified Coolant Pump with Insulator Plate

Figure 45: Final TMM Pump and Hardware Assembly

<u>Task 8: Inverter Design and Grid Interconnect – Plug Power</u>

Inverter efficiency testing was done to determine the potential performance of a 3-5kW 240V output transformerless inverter. The prototype inverter has a single half-bridge output stage. The input is a conventional boost converter. An additional half bridge generates a -200V rail from the output of the boost converter. It operates as a flyback converter running at 50% duty cycle.

The prototype was not designed to optimize all aspects of cost and efficiency. It was designed mainly from the viewpoint of rapidly proving the concept and providing a real-world validation of efficiency models.

Efficiency data for the prototype transformerless inverter was collected as well as baseline data from the P3 transformer-inverter (the standard Plug Power offering) and the European Delta inverter (Vaillant's European solution). Instrumentation used was a Yokogawa PZ4000 power meter with coaxial shunts and direct voltage connections. The dc input was wired to channel 1 and the ac output of the inverter was wired to channel 2. The wiring configuration was set to "1P2W-1P2W" to allow single phase efficiency (P2/P1) to be displayed directly. The PZ4000 was controlled via a Borland PC program that triggered the PZ4000 then collected relevant data and stored it in a .csv file for later analysis. This increased data capture speed and accuracy. The design initiatives to improve the prototype design during this program were as follows.

DFM: A modular board-centric approach is being adopted to eliminate complicated manual assembly. Leveraging a modular approach will allow for the new inverters to be configured as single phase 120VAC , dual rail 240V single phase, and three phase simply by stacking boards and using a common interconnect buss.

Embedded instrumentation is moving to less cable-harness centric design techniques, including embedded Hall effect sensors on planar magnetics, and a high speed digital interconnect to share sensor data among boards operating in a single inverter chassis.

Auxiliary plant load supply (24V) is being moved to a resonant synchronous current doubler topology, which is modeled to have a nominal efficiency of 94% and peak efficiency of 96%.

Efficiency: Additional efficiency is highly probable due to the redesign of front end converters. Previous design point of a 5kW converter and a 2kW balancer cascade led to a slight efficiency hit. These two converters are being replaced with dedicated 2.5kW-3kW converters, one for the +200V rail, and one for the -200V rail.

Cost: Moving to higher switching speed will minimize the size of magnetic components further reducing cost, and in many cases allowing the use of planar magnetics thereby eliminating the need to run heavy (approximately 4AWG) cable to these components.

Calibration Methodology
- The PZ4000 is operated with NOMINAL voltage and current calibration ratios (e.g., 50mV, 100A)
- The shunts were wired in series, with a 10A dc reference current run through them.
- 4 measurements were taken and averaged.
- The ratio of output current shunt measurement to input current shunt measurement is calculated as the “current calibration factor”
- The channel 1 and 2 voltage inputs wired in parallel
- 4 measurements were taken and averaged (2 are ac, 2 are dc)
- The ratio of average output Voltage measurement to input V measurement is the “voltage calibration factor”

Power and efficiency measurements are corrected by the product of the current and voltage calibration factors.

The total correction comes out to be about +0.5%.

The summary results are shown in Figure 46.

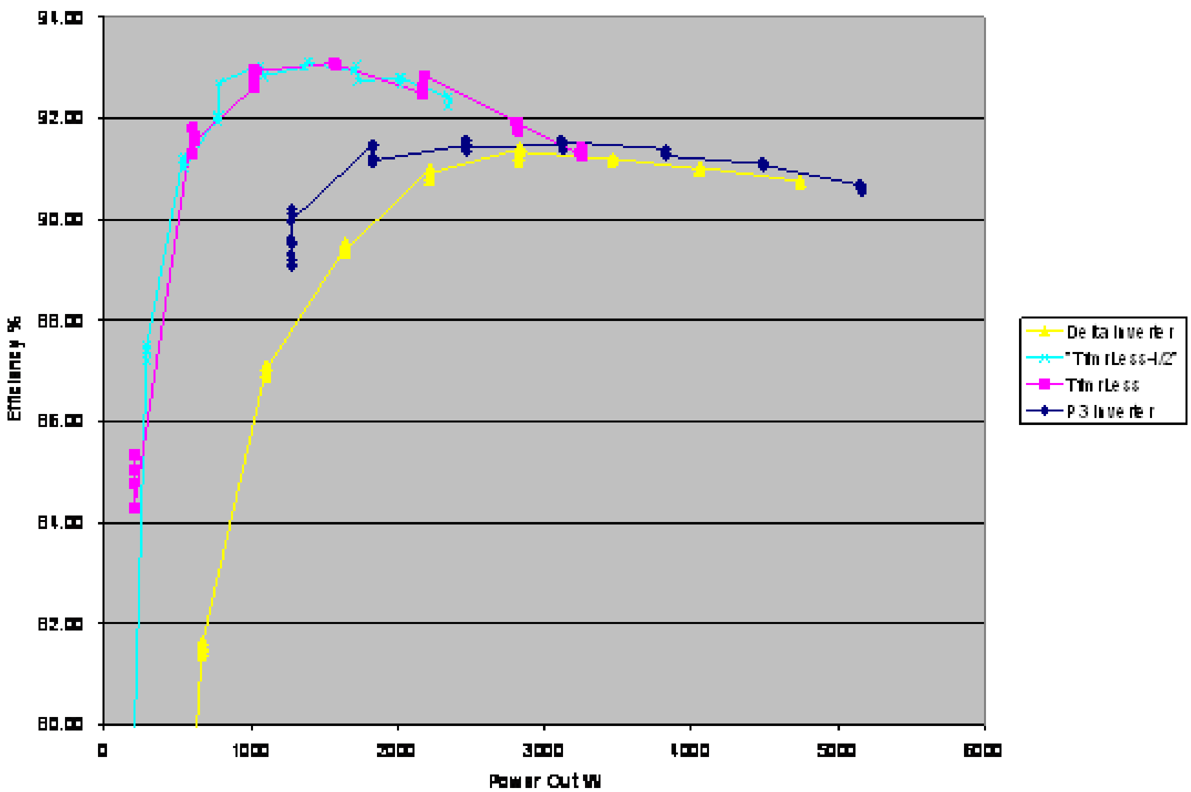

Figure 46: Inverter Efficiency vs. Power Output for Prototype Inverter and Baselines

The transformerless inverter had a peak efficiency of 93.5 percent at about 1200W. This is significantly better than both the P3 transformer-based inverter and the Delta inverter.

A 3-5kW version of the transformerless inverter could be expected to have a 4kW efficiency of 92% and a 6kW efficiency of 91.5% - both significantly better than the other inverters. These values can be obtained by doubling the power value on the chart above.

The transformerless inverter showed more variability that the P3 or Delta inverters in the test. This is due to an inadequate RF filtering at the inverter input and output, and software instability in the prototype inverter that caused HF noise every 450 ms. We thought it more important to collect data at this point than to hunt down the bug.

An initial set of runs was done at constant input voltage. This was however with a lower-current rated balancer inductor than the final curve.

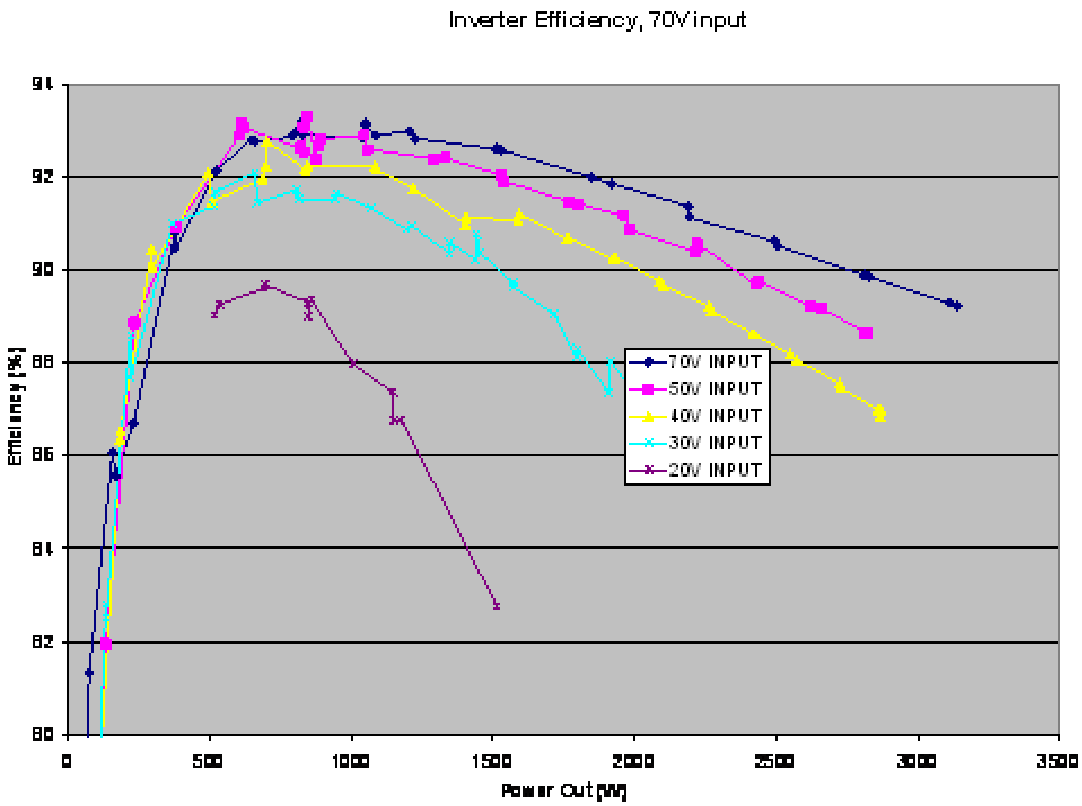

Figure 47: Prototype Inverter Efficiency vs. for a Variety of Input Voltages

A modular board approach is being adopted to eliminate complicated manual assembly. Leveraging a modular approach will allow for the new inverters to be configured as single phase 120VAC , dual rail 240V single phase, and three phase simply by stacking boards and using a common interconnect buss.

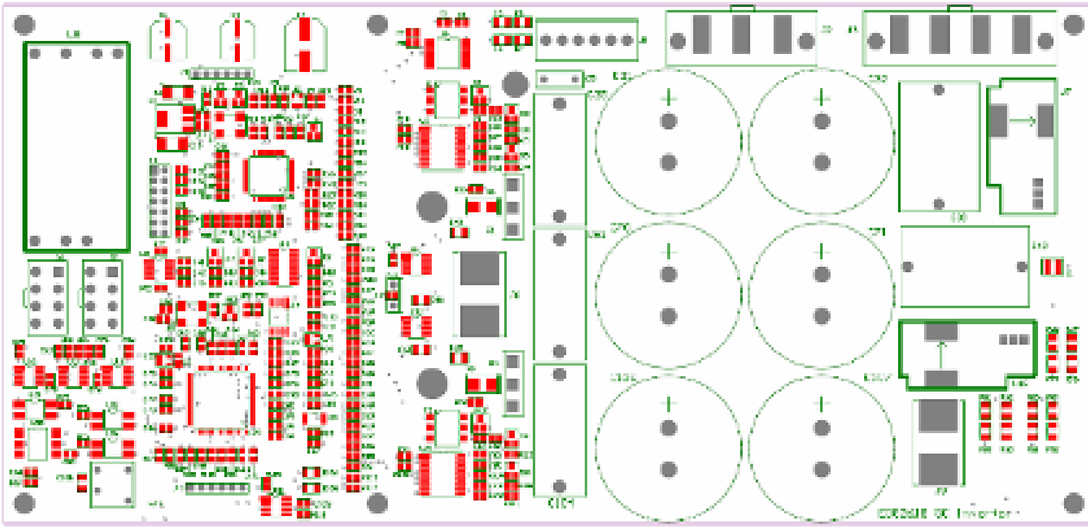

Figure 48: Single Phase (half-bridge) Inverter Board

Additional efficiency is highly probable due to the redesign of front end converters. Previous design point of a 5kW converter and a 2kW balancer cascade led to a slight efficiency hit. These two converters are being replaced with dedicated 2.5kW-3kW converters, one for the +200V rail, and one for the -200V rail.

A modular board-centric approach is being adopted to eliminate complicated manual assembly. Leveraging a modular approach will allow for the new inverters to be configured as single phase 120VAC , dual rail 240V single phase, and three phase simply by stacking boards and using a common interconnect buss.

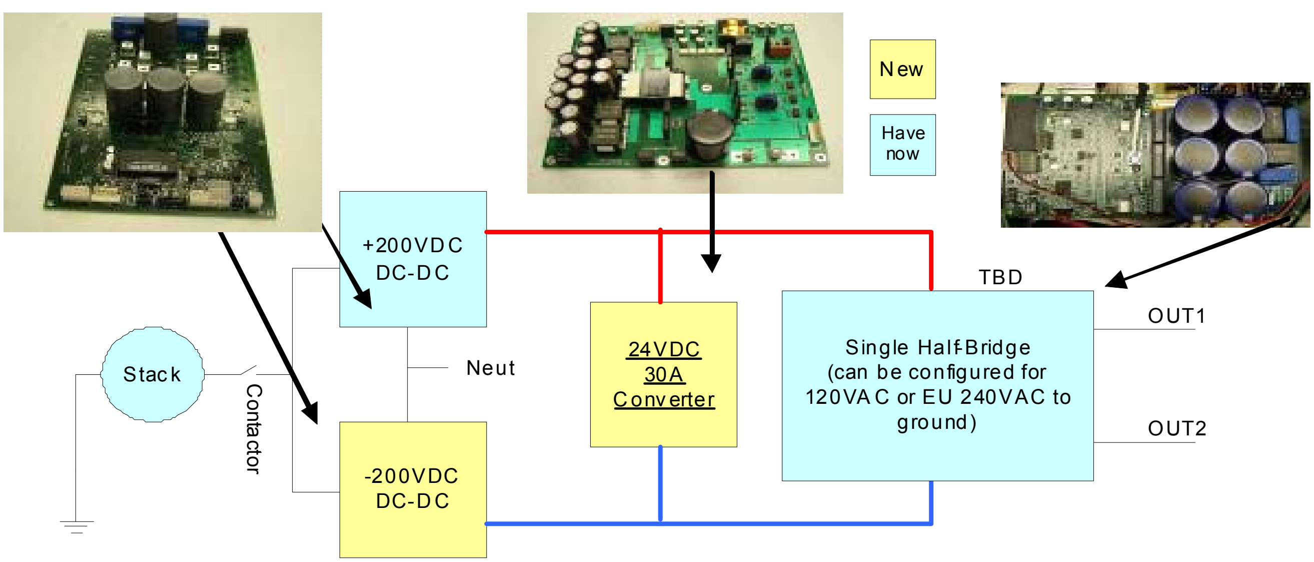

Figure 49: Inverter Solution Block Diagram.

24V Aux and Pump Module

Figure 50: 24V Aux and Module – Heat Sinks not Installed

The assembly, in its most general sense is a fully isolated quasi-resonant converter utilizing a synchronous current doubler rectifier to obtain the highest efficiency possible. The DC input can accept from 200-450V and it maintains .5% regulation and 100mV ripple over the whole load range. This assembly also features redundant safety features for over voltage, over temperature, and sustained overload faults. As the unit is powered by 400V, it was designed to meet UL 60-950 safety standards for "Reinforced Insulation 450V class" safety class. Outputs are fully isolated and floating, so they may be ground referenced to any point in the system. The transformer was designed to handle 1.68kW for future plant load requirements. A redesign and cost reduction are planned for this card.

Application Controller/Boost Flyback

Figure 51: Application Controller/Boost Flyback Board

The Application Controller is shown above and is based on a single TMS320F2808 32-bit DSP, which provides control and external communications for the complete system. The DSP concurrently controls Dynamic Current Limit, boost converter to 200V from fuel cell stack, and Flyback conversion to -200V. This will allow for easier UL certification of the inverter assembly as a whole. The inverter card code can be "locked" early on, as its function is very clearly defined, and only code changes to the application controller – which have no UL visibility – will need to be considered for any functional improvements/customizations.

The application controller comprises:

- A 2.5kW boost converter that feeds 55-85V fuel cell power to the +200V system DC bus.
- A 2.5kW flyback converter that feeds 55-85V fuel cell power to the -200V system DC bus.
- A Texas Instruments TMS24LF2808 Digital Signal Processor (DSP) chip that acts as both general application controller and local power-electronics controller
- Two CAN communications ports for external communications with the system and internal communications with the inverter boards and other future BOS equipment. The external CAN port is galvanically isolated.
- One galvanically isolated RS485 port for external communications. This can be configured to use Plug Power's Standard Inverter Protocol (SIP).
- Internal monitoring of fuel cell and bus voltages.
- Control and state-monitoring for an optional Gigavac main fuel cell contactor

Inverter Controller

Figure 52: Inverter Controller Board

The inverter module board is capable of 3KW of output power and is of the modern utility interactive transformerless "half-bridge" type with an LC output filter. This topology reduces mass significantly, as there is no 42kg transformer at the output stage. For 120VAC applications, a single half bridge is used. For 240VAC applications, a pair of these boards are used controlled out of phase to provide a true L1-N-L2 power source.

This filtered chopper approach allows this part of the inverter to be entirely machine assembled and purchased as a finished module, ready to receive a simple wiring harness for interconnect.

Each module features phase angle control for EPS/Stand Alone mode, such that two units connected will always come up 180 deg out of phase producing 240VAC line to line.

The inverter card has a 3kW single phase half-bridge inverter consisting of two IGBTs and associated gate drive circuitry. It uses a Texas Instruments TMS240LF2810 DSP device as the main controller and TMS240LF2403 as a slave. The slave processor is used for redundant monitoring which may be required for safety certification. The inverter card also has external safety-shutdown and phase-control ports, and one isolated CAN communications port.

The AC output supports both stand-alone and grid connect modes. A sealed (Gigavac) contactor is supported for the grid-connect contactor so that the complete unit can maintain Class 1 Div II classification. Output filtering is provided via external inductors and a commercial RFI filter.

Prototype

The inverter module consists of the inverter card, inductor and heat sink. The heat sink used in the prototype is much larger than needed and can be reduced for size and cost. The stand alone inverter module used for testing is shown below.

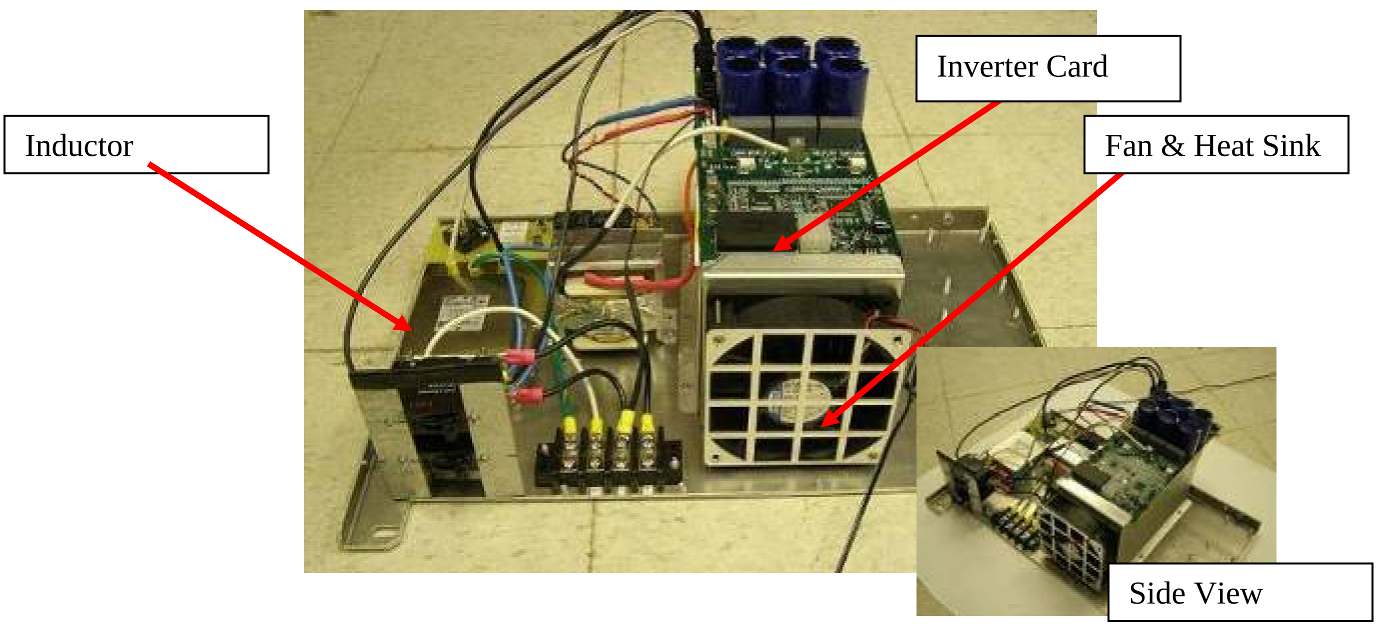

Figure 53: Inverter Module – Front and Side Views

Testing:

Each module was tested for basic functionality and then sub-systems were tested for efficiency. The transformerless inverter was first tested with a single inverter stage up to 3kW output power, and then with two stages up to 5600W. Input DC power was provided by an Electronic Measurements (EMC) 100V 300A lab supply. The inverter load was a Simplex load bank that allows 250W steps at 120V and 500W steps at 240V output.

All dc and ac measurements were taken with a Yokogawa PZ4000 0.2%dc/0.1% ac accuracy power analyzer. T&M Research high-accuracy coaxial shunts were used for all current measurements

The efficiency measurement system was calibrated by applying the same dc current (100A) to all shunts, and the same ac and dc voltages to all voltage inputs. 10 x 1-second readings for each voltage and current were taken and averaged to generate the overall power calibration factors.

Efficiency was calculated as Pout/Pin using the PZ4000 true power measurement capability. 10 measurements were taken at each output power and input voltage point to allow variability to be assessed. The inverter stage efficiency was measured by inserting current shunts in the +/-200V dc lines from the Controller to an inverter stage. These measurements showed more variability than the input and output power measurements due to the common-mode noise injected from the DC busses.

The aux converter was tested with 400V dc input provided by the Sorenson SGA600/17 supply and loaded with the Kikusui >PL21004W load bank. All measurements were taken with precision shunts and BK precision 5Y92 GPIB multimeters. The pump converter used the same test setup, but with 200V dc input (due to the non-optimal transformer turns ratio).

The test equipment list is shown below:

Multimeter BK Precision 5Y92
Electronics Load Bank Kikusui PL21004W
Electronics Load Bank Kikusui PL22004WB
Power Supply Sorenson SGA600/17
Power Analyzer Yokagawa PZ4000
Oscilloscope Tektronix TDS3034
Load Bank Simplex Swift-e F.T.
High Voltage Tektronix P520J
Differential Probe
T&M Research (Alb. NM) coaxial shunts

24V Auxiliary Board and Pump Board Stand Alone Testing:

The 24V Aux board was tested independently from +/- 200 volt rails to provide the following efficiency data.

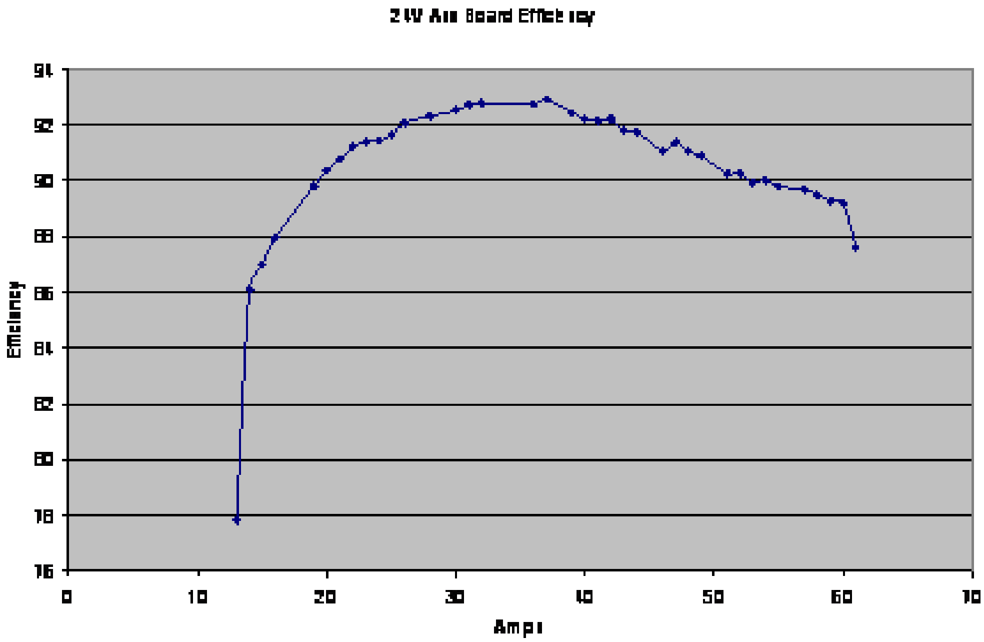

Figure 54: Aux Converter Efficiency.

Single Inverter Stage Testing
A single Inverter stage was tested individually at 120V output. The results are shown below.

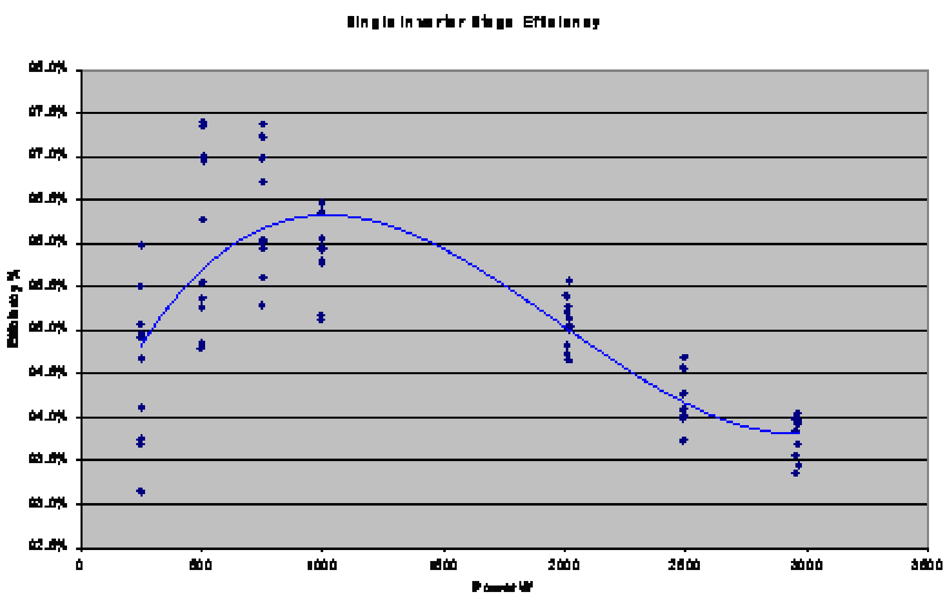

Figure 55: Power Inverter Efficiency

The peak efficiency for this stage is between 500 and 1000W. The shape of the curve can be attributed to three components:

- Constant or tare losses. These were measured at about 20W for power switching and 15W for housekeeping (control and measurement) power.
- Proportional losses. These come from constant voltage drops in switching devices such as IGBTs, and switching losses that are proportional to current. Proportional losses are about 100W for the total system at full power.
- Square losses. These are due to resistance in all power circuits, but mainly in wiring, inductors, and FET switches. These total to about 200W for the full system.

At low power, the tare losses dominate, and efficiency falls rapidly as load approaches zero. In the middle range, proportional losses have most impact, while square losses dominate at high power. Comparison to the previous inverter using the same test setup and calibration is shown below.

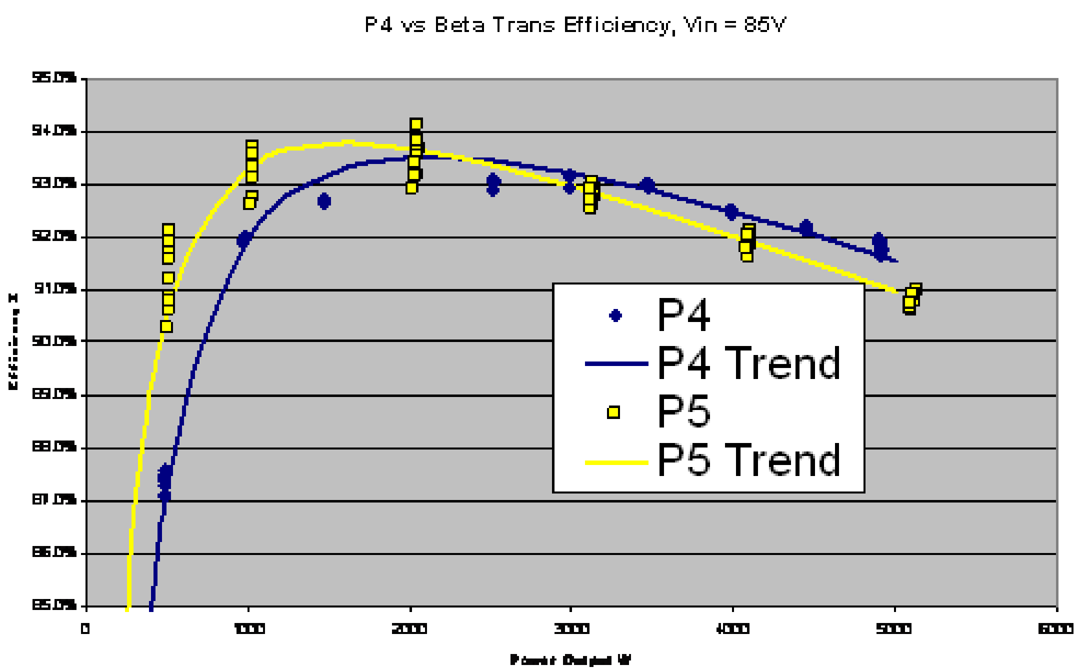

Figure 56: Comparison of Previous Generation Product to New Design

During the program, efficiency Improvements including reduction in tare losses, reduction in IGBT and switching losses and the reduction in resistive losses improved the peak efficiency in excess of an additional 1% to a peak of over 94% at approximately 2kW.

A DMC analysis was completed comparing the P4 inverter and the Transformerless Beta. This estimate shows a cost savings of more than 30% over baseline. Additionally, P4 is 53% smaller in volume and 67% less in weight.

Task 9: Software Controls and Development – Plug Power

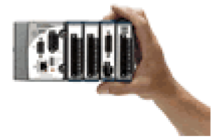

One of our goals was to find a robust stand-alone controller that would allow us to continue developing controls in the methods which we have in the past. After evaluating several controllers we decided on using National Instrument's Compact Rio platform. It is a flexible, modular programmable automation controller with limited risk to migrating over.

The team worked with Brownlie Design to come up with a new customer user interface. This will allow for come basic feedback information to the customer along with some basic controls. The customer interface allows the user to turn the system on and off, toggle between heat only and CHP modes and provides data on thermal power output, electrical power output and overall system efficiency. The interface will also tell the user if maintenance is required on the system.

Air Delivery Module Controller Development: We developed the air delivery module and controller in conjunction with the Institute Jozef Stefan in Slovenia to develop a "smart controller" for our air delivery module. Together, we developed a module which included all necessary electronics and controls associated with the Air Delivery Module.

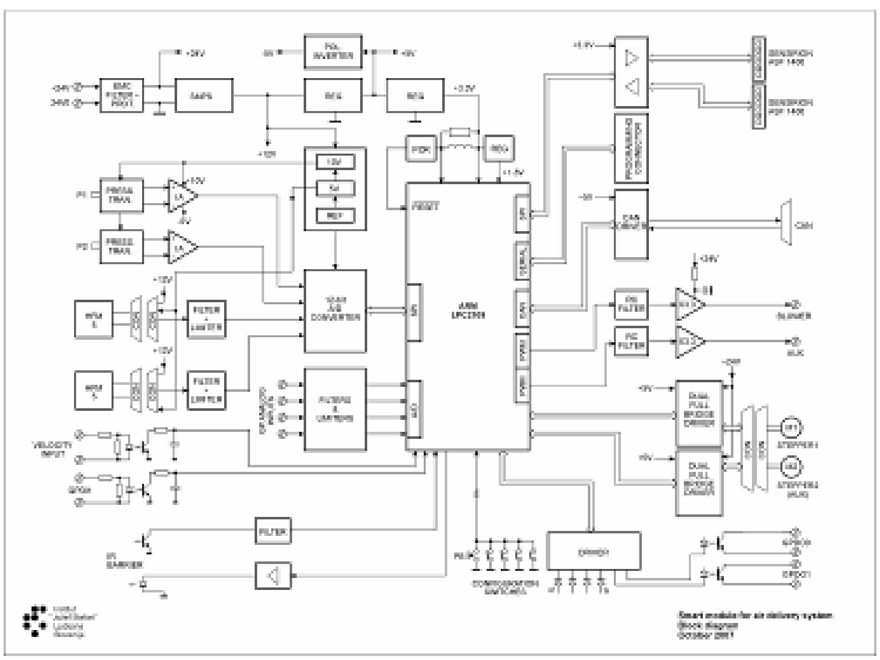

Figure 57. ADM Controls

A second task associated with the Air Delivery Module is working in conjunction with Domel on a new manifold and blower design. Domel is developing a multi-phase controller, which will improve efficiency along with a simplified single stepper manifold.

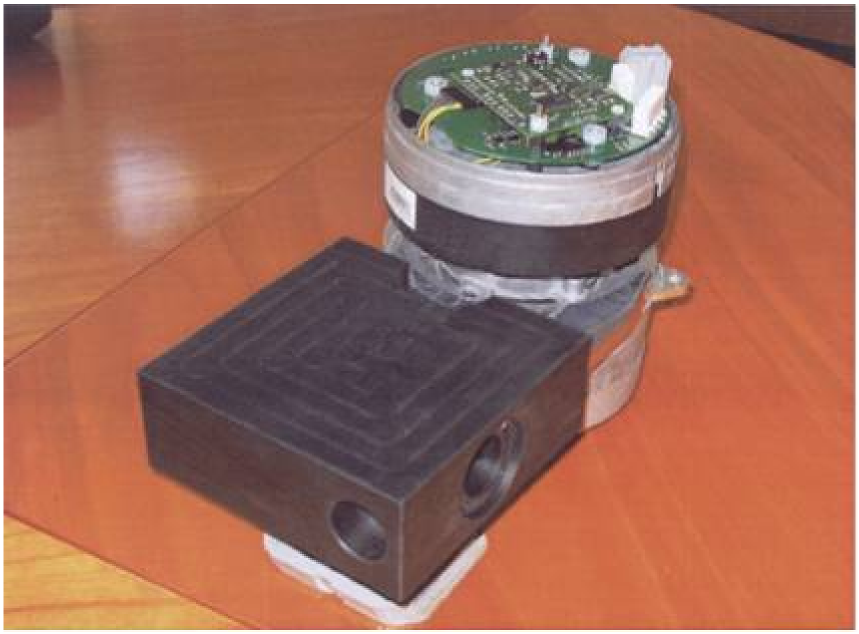

Figure 58: Air Delivery Module

Controls development work this quarter included a number of electrical board designs and verifications. Below you can see the electrical layout of two PC Boards which will be used in the new system. The customer interface layout includes three sets of numerical indicators and bar graphs to show how the system is performing, startup and shutdown controls, and mode indicators and maintenance indicators.

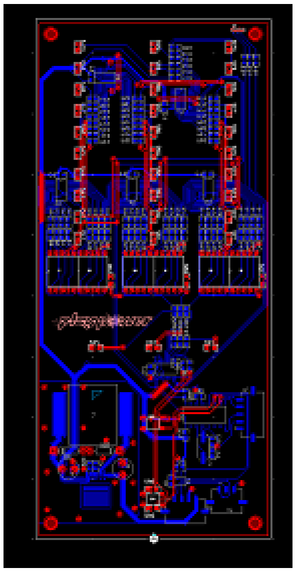

Figure 59: Epsilon User Interface

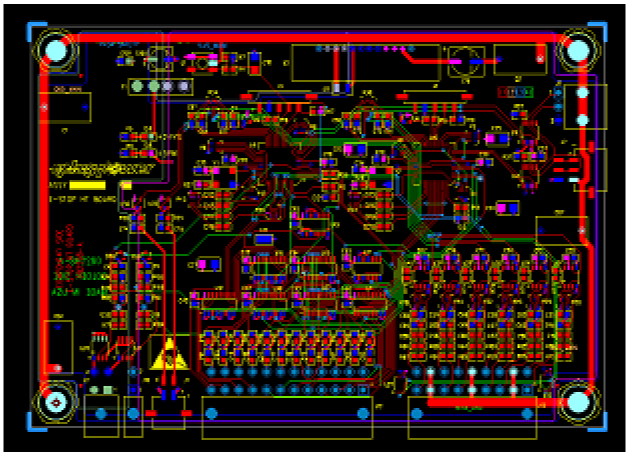

Figure 60: Emergency Stop Board

We also developed a new Emergency Stop board which will control all the system safety's and have the ability to shutdown the power to the system. The new design was developed to include double redundant safety control by two separate processors.

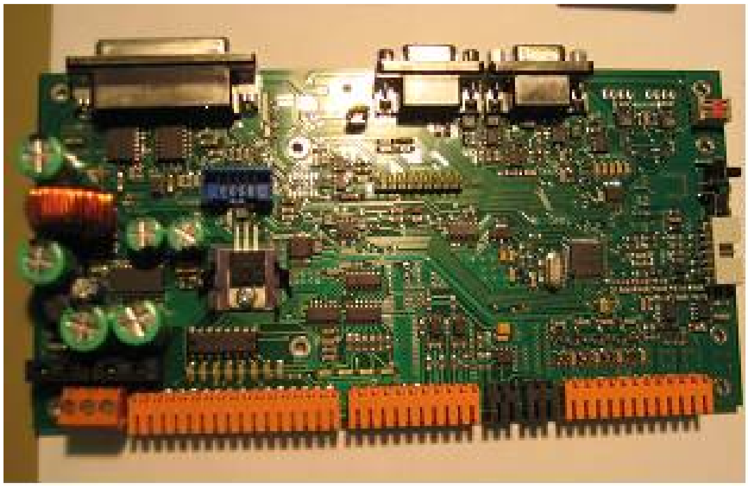

Figure 61: Air Delivery Smart Module

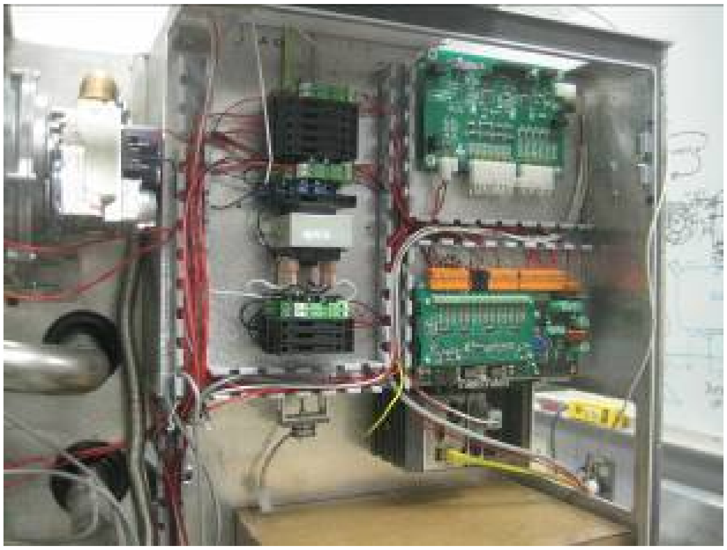

Figure 62: Final Board Layout and Assembly

Figure 63: Final User Interface

Controls development continues with the characterization of the components in the fully assembled system

Task 10: Integrated System Design – Plug Power

Plug Power has continued the system design activities that originated in the NIST & NYSERDA Programs, advancing the “Delta” system to the new “Epsilon” configuration. The new configuration is 25% smaller by volume, while incorporating additional functionality.

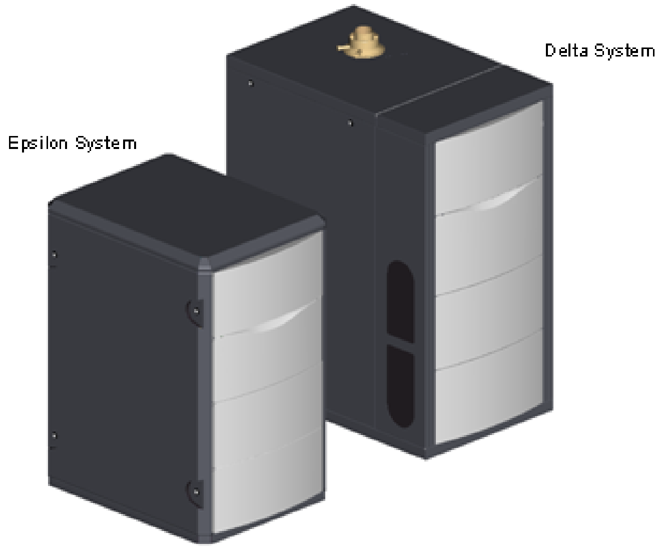

Figure 64: Epsilon vs. Delta System

A key aspect of system configuration is the separation of hot side and cold side components to provide for maximum total efficiency and long component life. The hot environment around a fuel cell stack or reformer is not well-suited for motors or electronics. Additionally some mechanical subsystems (desulphurization, air filter) perform significantly better under low ambient conditions.

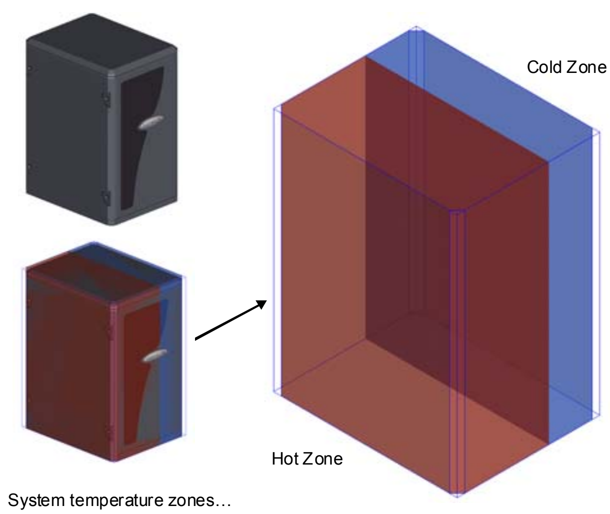

Figure 65: Hot and Cold Zones in the Epsilon System

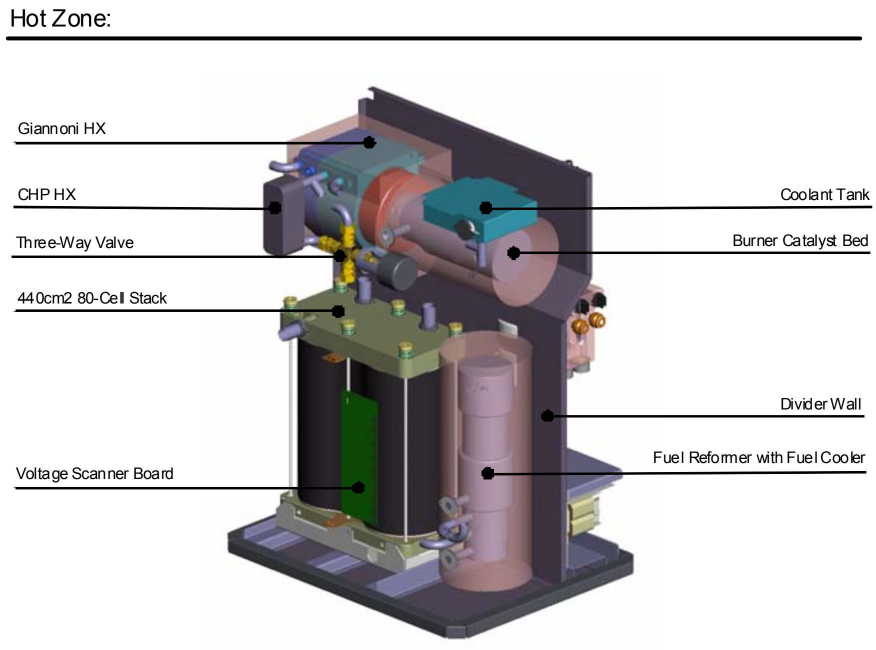

Figure 66: Epsilon System Packaging Concept Hot Side

Figures 66 and 67 illustrate the final packaging concept which allows for easy serviceability and installation flexibility. From this illustration you can identify the fuel cell stack, reformer, integrated peak heater, desulphurization beds, inverter, and balance of plant components.

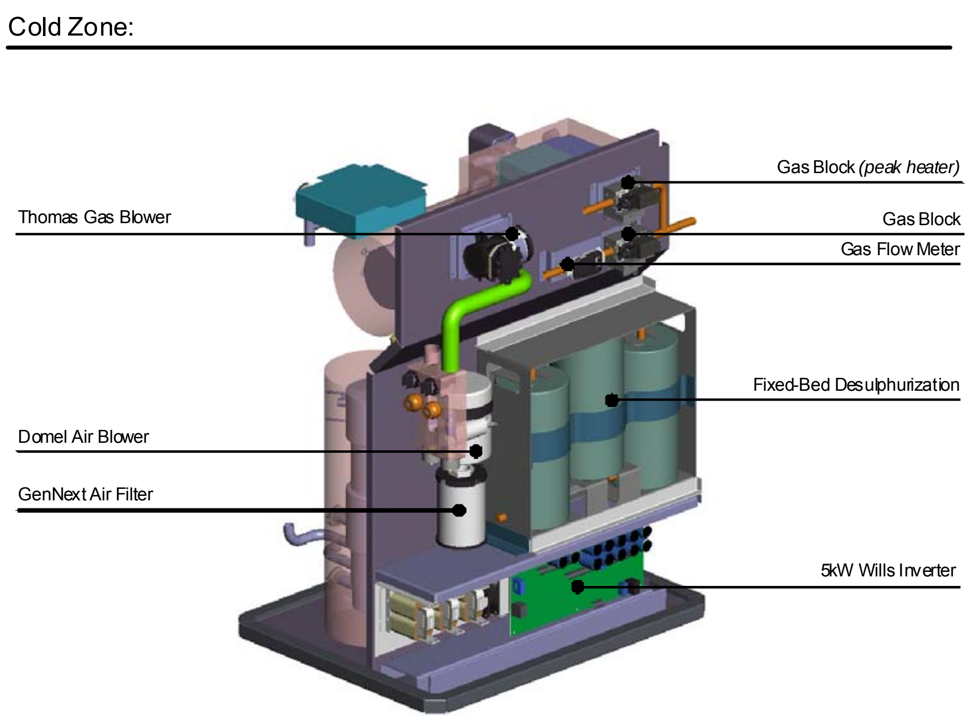

Figure 67: Epsilon System Packaging Concept Cold Side

The goal of this system build was to scale down, increase manufacturability, serviceability and make components more modular. We have reduced the system size by another 25% and continue to improve the way we assemble, pipe and insulate the system. System thermal efficiency is improved due to less wasted area and increased component insulation. DMC has been reduced by 50% over previous builds. We have worked closely with Brownlie Design to make this system an esthetically pleasing and unique look.

Figure 68: Integrated System Model

Figure 69: System Hardware in Assembly

Task 11: Fuel Cell System Build and Verification Test – Plug Power

A TMM test rig was designed and built and continues to provide life and controls data. This test rig confirmed component performance, allowed for controls development, supported pump endurance testing, and allowed for alternate coolant testing as backup to the prime path coolant.

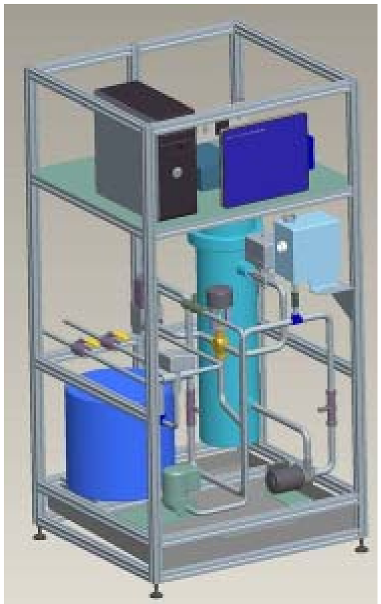

Figure 70: TMM Rig

Rig data includes 8 pressure transducers, 7 thermocouples, and 3 flowmeters all logged to a DAQ with network access.

Air Delivery Module

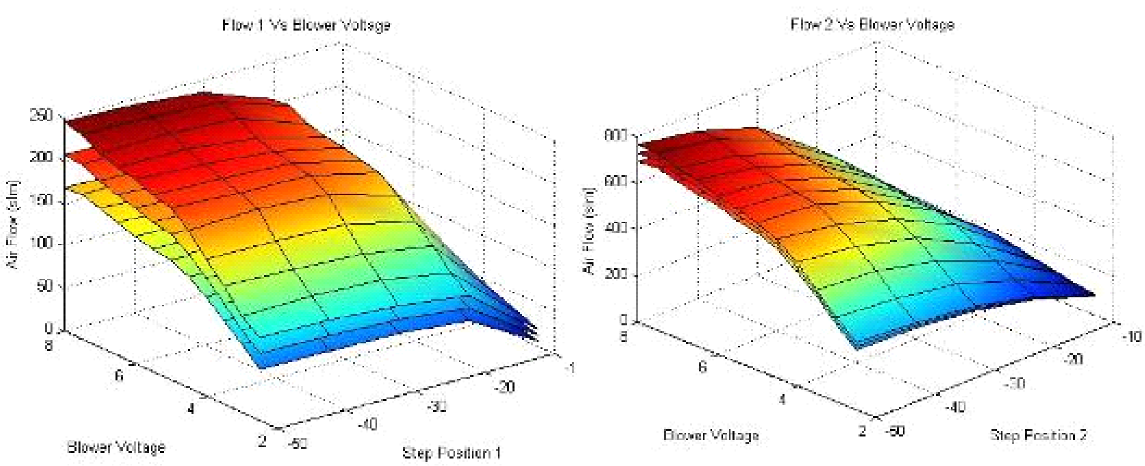

Figure 71: Flow and Variability for Air Delivery Module

Plug Power worked with Domel to develop a new, integrated air delivery module as well as an advanced internal air delivery module controller. Detailed FEA analysis has been performed on single and double stepper configurations, and full characterization the blower has been performed. Both Plug Power and Domel, via the Josef Stefan Institute have characterized the hardware and contributed controls development to the full integrated module. Figure 71 demonstrates the multivariable performance mapping that is used to generate feed forward control models of the air delivery module.

Figure 72: Air Delivery Module Rig

Fuel Delivery Module

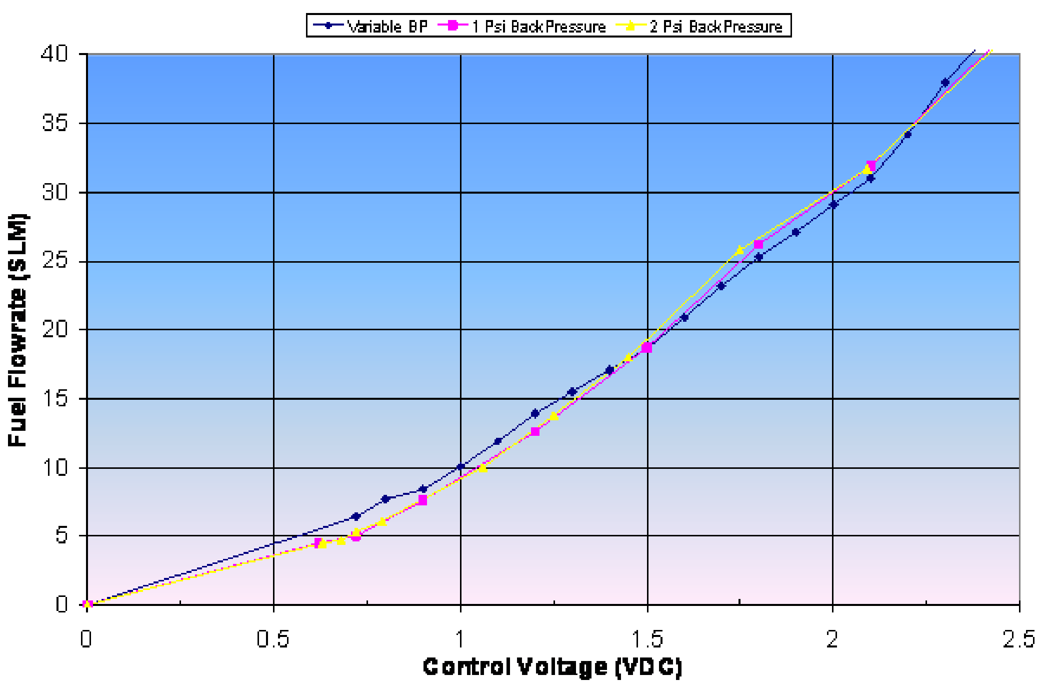

Figure 73: Flow and Variability for Fuel Delivery Module

Since standard line pressure of natural gas is between 4 and 12 inches of water, the FCHA must increase this pressure to overcome pressure drop through the reformer, stack and exhaust components. Stability and consistency of the fuel flow to the system are vital to smooth operation, and low degradation rates. Since the fuel blower is substantially smaller than its air counterparts, pressure oscillations within the system are prone to causing reflected disturbances in the fuel flow, which manifest themselves as cyclic variation in reformer temperature, and electrical production from the fuel cell stack. Plug Power has been evaluating a new diaphragm based blower for potential application as the fuel delivery blower which demonstrates robustness against anticipated changes in system backpressure. Figure 73 show the flow versus control voltage for this new blower at variable backpressure and with fixed high/low back pressures.

Integrated Supplemental Heater

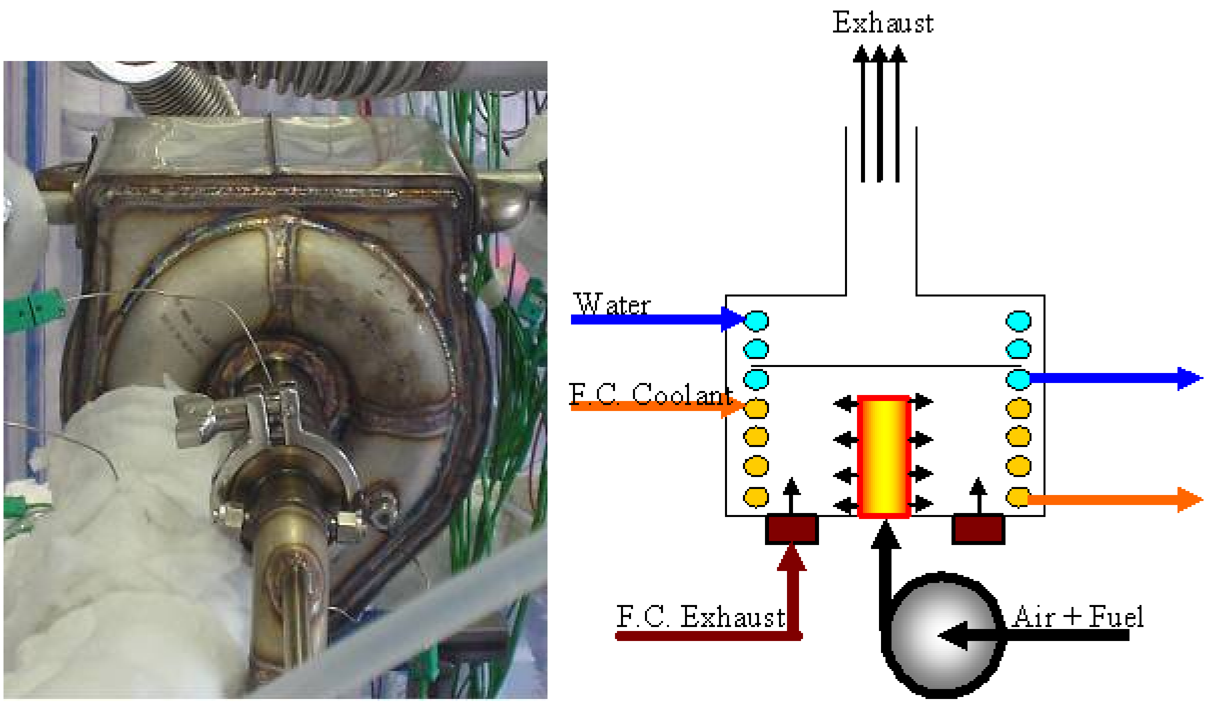

Figure 74: Burner and heat exchanger configuration

Burner testing was performed by feeding air and fuel at ambient temperature into the burner head. Simulation of ATO recuperator exhaust was done by introducing heated nitrogen into the second burner feed. The reformate in reality has H2O, CO2, N2 and O2 as the bulk composition, however as it is not passed into the reaction zone of the flamelets, thus it does not act as a diluent in the reaction zone. N2 is thus adequate for simulating the disturbance of the flow patterns in the burner, as well as the quenching of the reaction at the mixing interface. Performance of the burner was tested at startup conditions, as well as operating conditions. From operating conditions there are two variables we scanned. One is the AC fuel cell capacity, and the other is the thermal peak fuel burned in the burner. For example, we operated the burner at simulated reformate exhaust levels of 3 kW AC (this is approximately 300 slm of N2 equivalent at 450°C introduced into the burner. At the same time we would try to light the burner by turning on air first, then sparker, and lastly fuel. For simulated fuel combustion of 25 kWth for example, we would add 500 slm air and then introduce 42 slm of CH4 after the sparker has been initiated. Ignition was detected by a thermocouple temperature rise (the thermocouple was located in the combustion chamber). Once the ignition is detected, the sparker was turned off. Typically, sparker was turned off within 10 seconds.

Figure 75: Peak Heater Module in Integrated Test Rig

The team built three systems: E1, E2 and E3. The missions for these systems were as follows:

- E1 – Plug Power labs and controls optimization. This system remained at Plug Power and underwent endurance testing and advanced controls development.
- E2 – Trade shows and Apeldoorn labs. E2 was sent to represent the program at the Hannover Fair in Hannover Germany in April 2008. It then returned to Plug Power for commissioning. After debug it was sent to the Plug Power Apeldoorn facility for endurance testing and system testing for technology initiatives that didn't make it into the final system design such as hydrodesulfurization of the natural gas feed.
- E3 – Vaillant labs. This system was commissioned at Plug Power and then sent to the Vaillant labs in Remscheid, Germany for customer testing.

Below are pictures of the E1 build beginning with the unpainted enclosure and followed by a picture of the system components and of the build itself. Note the relatively small number of components required by the high temperature system. The simplicity of design allowed by the technology is striking.

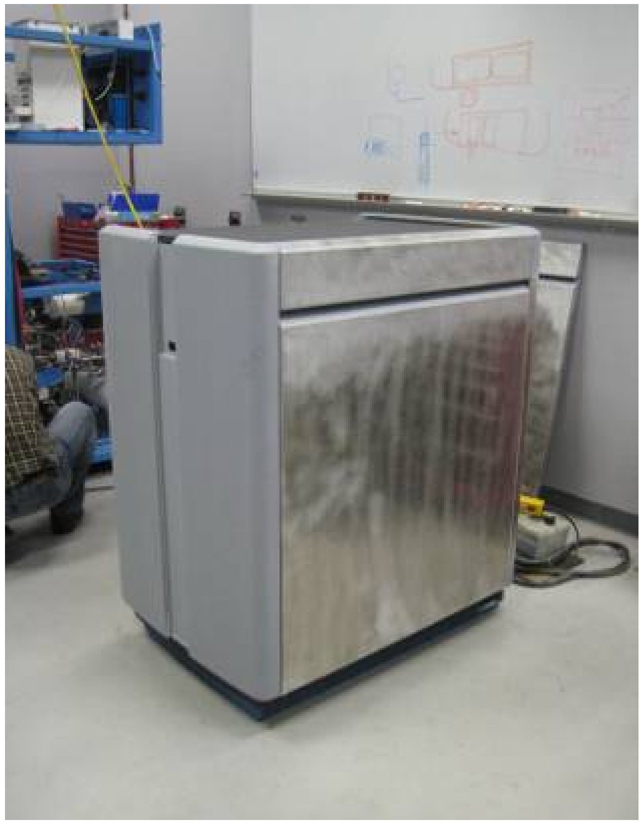

Figure 76: Unpainted System Enclosure

Figure 77: Total System Hardware

Figure 78: E1 System Final Assembly

Figure 79: Finished System on Display at the Hannover Fair

On display at Hannover, the system was seen and evaluated by US and EU officials and natural gas and related industry VIPs from around the world. It was positively received and has generated a variety of technology and business development negotiations: everything from stack and component collaborations to system field trials and spin off products. The impact of this transatlantic program to the entire fuel cell industry value chain, from component suppliers to end users, cannot be understated. It will have lasting, beneficial consequences long after the program is contractually completed.

Task 12: Fuel Cell Demonstration Test – Plug Power et. al.

Below is an example of Epsilon 1 (Plug Power Latham) running in steady state mode for a one week test. The system averages approximately 30% electrical efficiency at the 1.5 kW setpoint. This efficiency is expected to improve once the system controls are optimized.

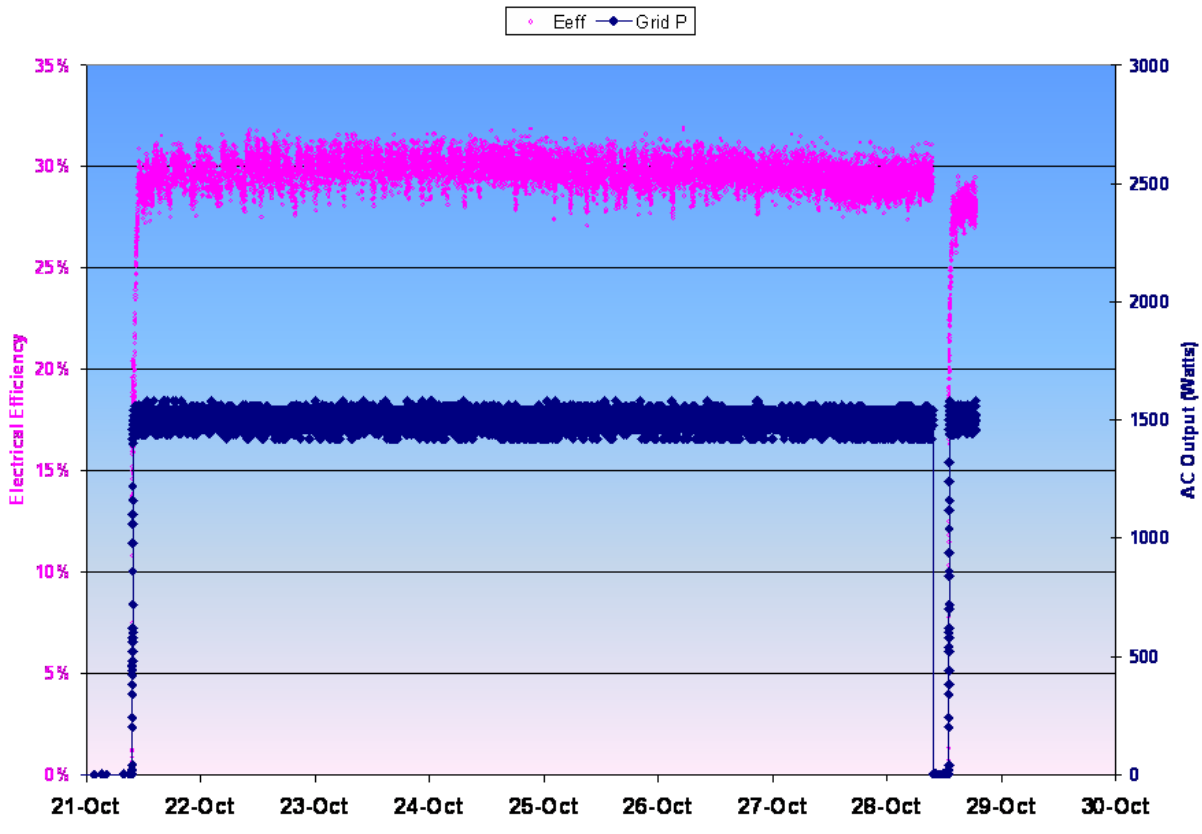

Figure 80: Sample System Operation

During the program, Epsilon 1 in Latham has accumulated over 3000 hours of run time. Epsilon 2 accumulated over 800 hours in Apeldoorn and Epsilon 3, to date has achieved just less than 4000 hours at Vaillant in Germany. See Figure 81. Aside from intentional shutdowns to incorporate software and hardware changes, the majority of system trips have been due to lab issues and personnel error. The number of systems trips due to hardware and software malfunctions have been small.

A major system operational issue has been around the control of the reformer. Optimizing between the air flows to the stack and to the reformer is a major control challenge in the system. Misoperation of the reformer leads to high concentrations of CO in the reformate to the stack which leads to poor stack performance. One of the advantages of the high-temperature PEM technology is it's resistance to CO poisoning but CO still has a negative impact on stack performance. There is a design balance between the complexity of the reformer (number of reactor beds, amount of steam available) and the performance of the stack. The optimum system target is 1% CO in the reformate from the reformer.

During initial debugging the reformer was operating at 4% or greater CO thereby causing the stack to be operating poorly in terms of efficiency and max power output. Software optimization has brought the reformer back to its 1% target that we can repeatable achieve in ex situ testing.

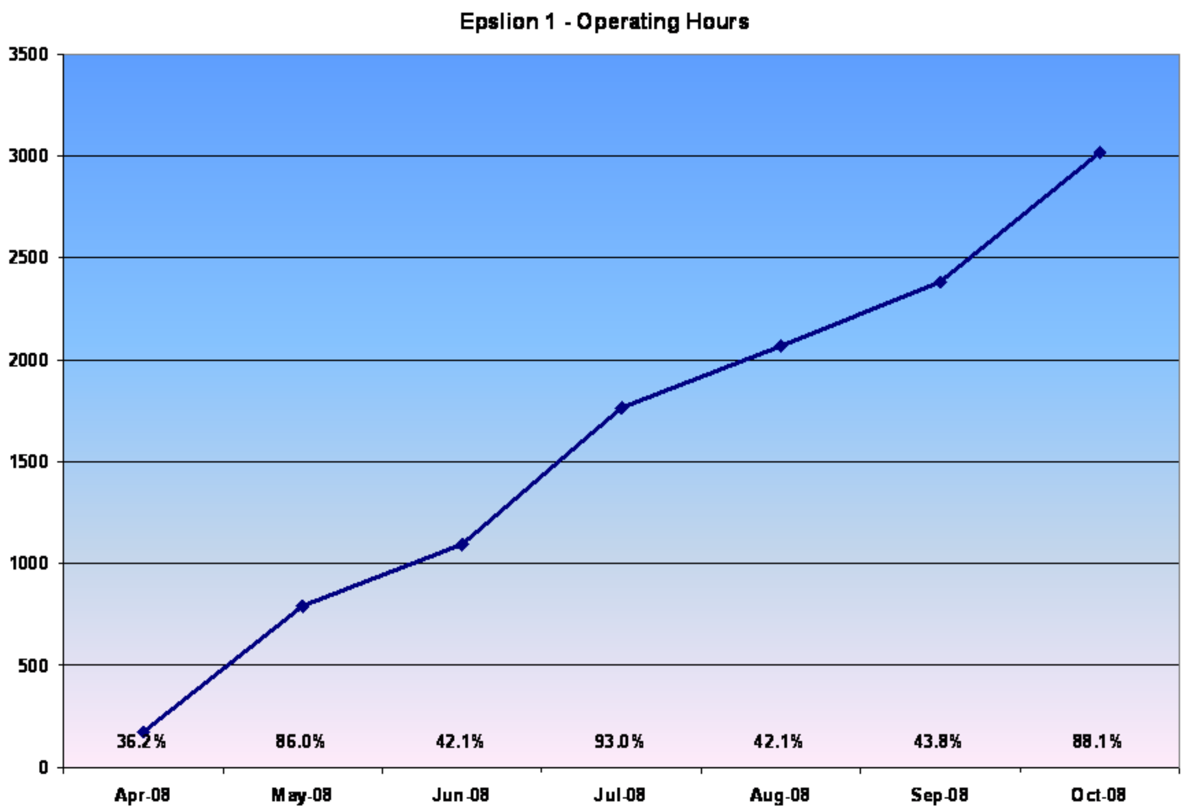

Figure 81: Epsilon 1 Cumulative Run Hours

Another advantage to the high temperature system design is its ability to rapidly startup since the integrated burner can heat the system up quickly. See Figure 82. Notice the rate at which the stack temperature can be increased around the three minute mark.

We have intentionally limited the rate of heat up until we can better understand the thermal stresses involved in a very rapid fuel cell start but with the integrated burner, the system has the capability to start in less than 15 minutes. Current baseline is a 40 minute startup.

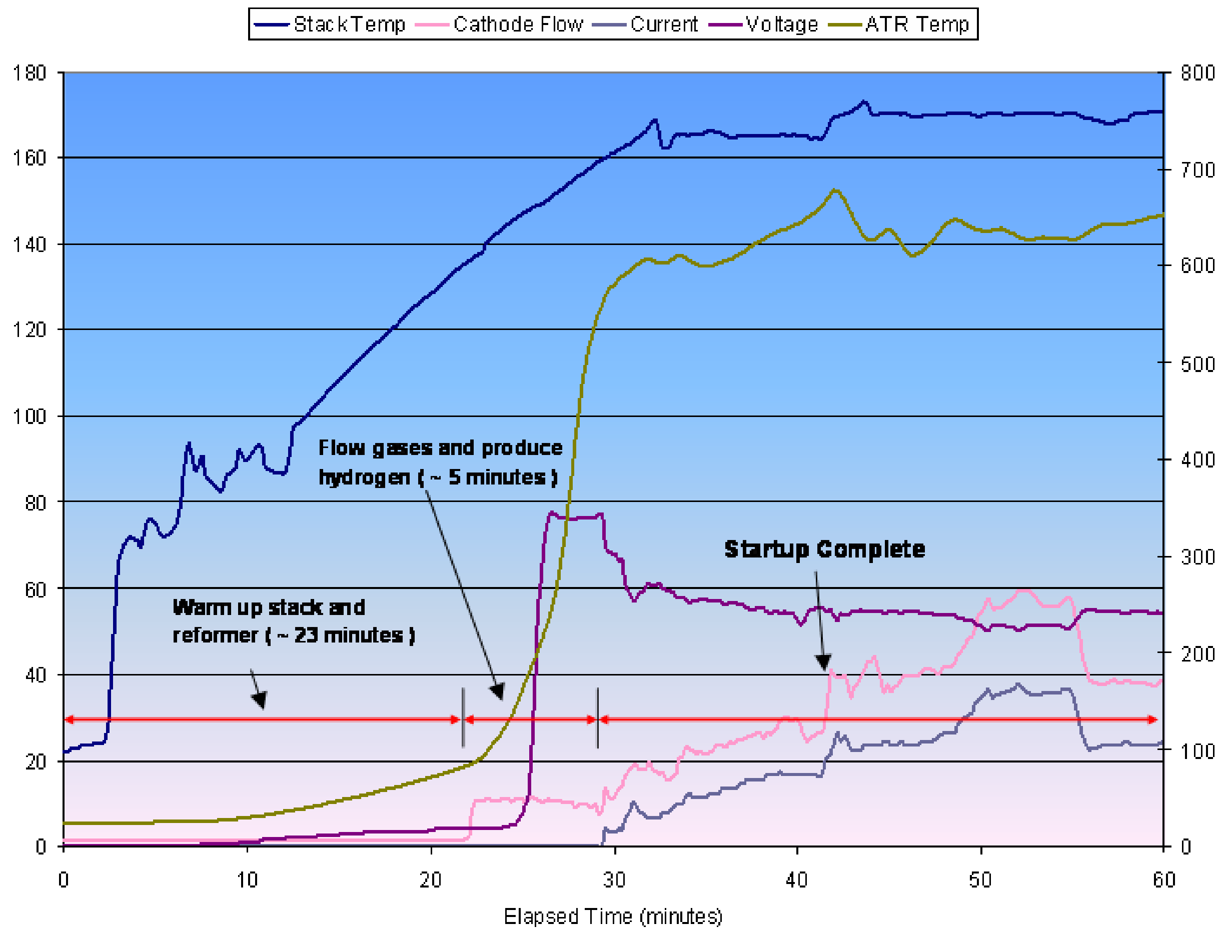

Figure 82: System Start Up Example

The system has responded well to transients and load following as shown in Figures 83 and 84 below. While load following is not critical to operation in a grid parallel system it is important for overall system efficiency and return on investment to the customer: it is best to use as much of the low cost natural gas as possible in order to offset the cost of high priced electricity. This will also be important for follow on designs allowing off grid applications.

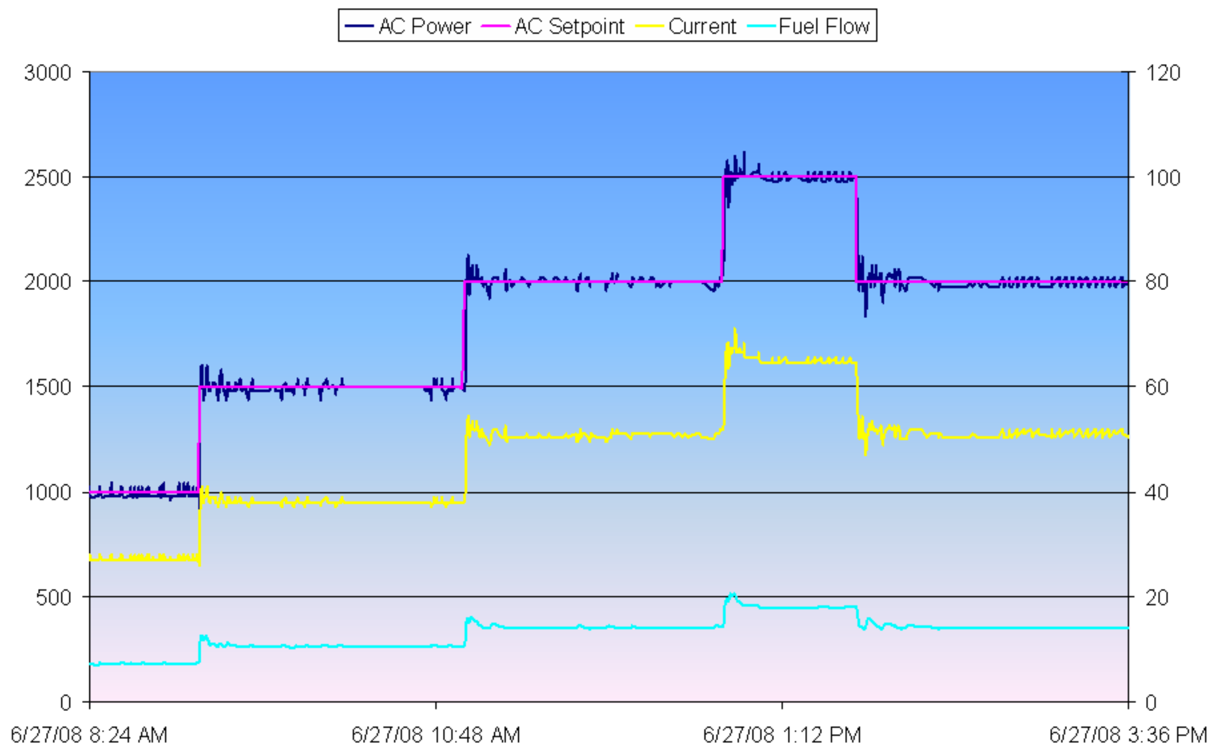

Figure 83: System Load Following

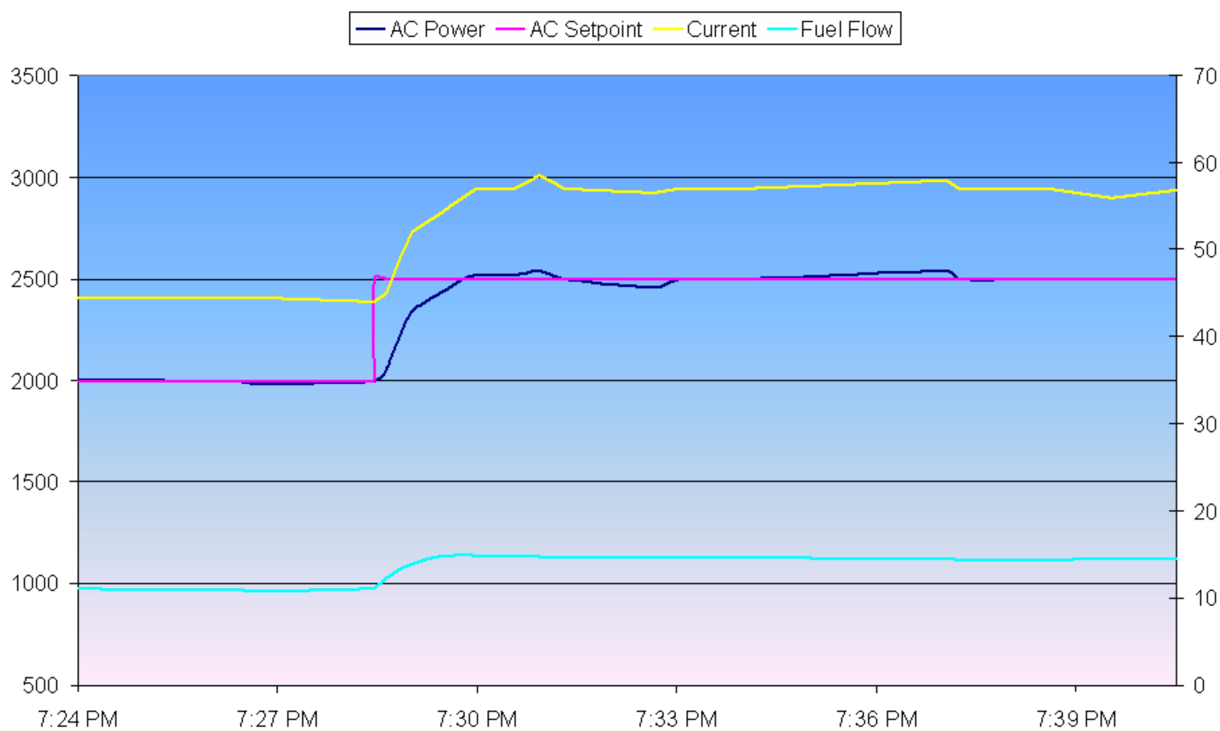

Figure 84: System Load Changes

Detailed efficiency measurements have been taken and are shown below. The data in blue represents system performance with the current inverter while the red data shows projected system performance with the optimized inverter based on bench data from inverter testing.

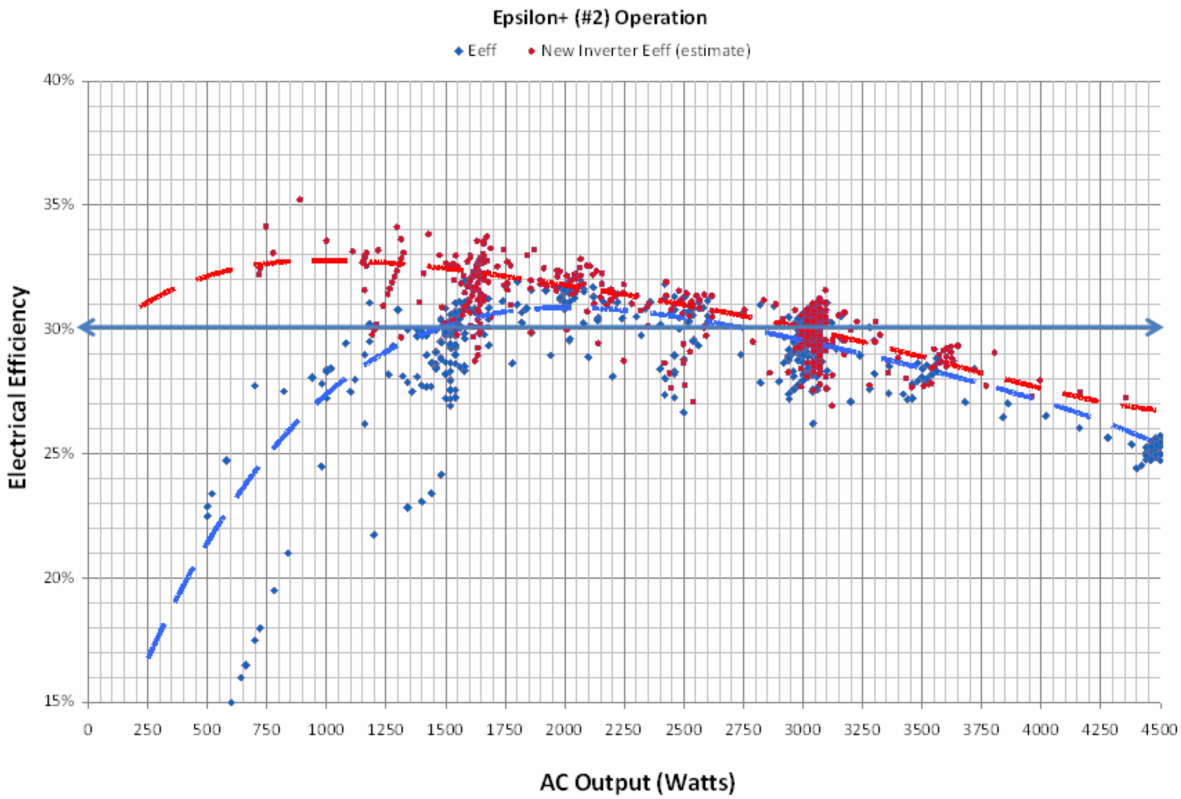

Figure 85: System Performance vs. Output

Another area developed and explored at length is controllability of the system during transients. It is important to have stable system operating conditions while changing load. Most of the controls development effort has been spent with this objective. Below is a graph showing critical system performance measurements as functions of AC load demand changes.

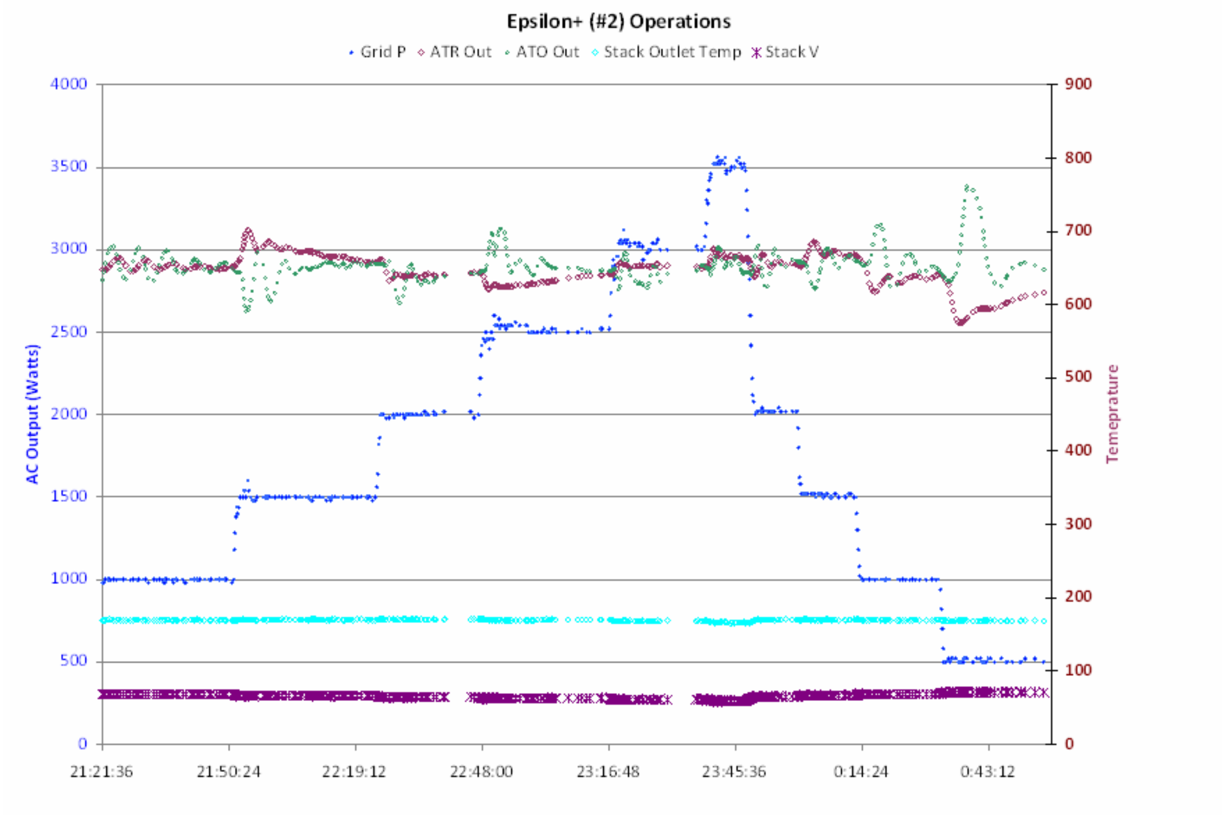

Figure 86: Critical System Parameters as a Function of Load Changes

Conclusions:

This was a very productive, successful program. The interactions and development efforts with our EU partners led to increased learning and sharing of ideas. We should make every effort to continue developing international collaborations in programs such as this.

This program has demonstrated the viability of developing fuel cells as residential appliances. As MEA, stack and system development and refinement continues, reliability will improve, costs will continue to be drastically reduced and functionality will be introduced that will make this technology the natural choice for micro-cogeneration of heat and power in the home or light commercial application.

There are significant areas for continued improvement. We have not approached the limits of this technology in this program. Membrane improvements, catalyst stability, platinum loading, system integration and control are barely out of the prototype stages. Production engineering, volume manufacturing and productization will drive improvements that will benefit the entire industry.

Patents:

None

Publications:

None

Presentations:

- DOE 2008 Annual Merit Review: FC40 – International Stationary Demonstration Program; John Vogel
- DOE 2009 Annual Merit Review: FC40 – International Stationary Demonstration Program; John Vogel